

---

# MINING OF SINGLE-CLASS BY ACTIVE LEARNING FOR SEMANTIC SEGMENTATION

---

• **Hugues Lambert**  
GSK.ai, GSK plc  
NIC 4AG, London  
<hugues.c.lambert@gsk.com>

• **Emma Slade**  
GSK.ai, GSK plc  
NIC 4AG, London  
<emma.x.slade@gsk.com>

July 19, 2023

## ABSTRACT

Several Active Learning (AL) policies require retraining a target model several times in order to identify the most informative samples and rarely offer the option to focus on the acquisition of samples from underrepresented classes. Here the Mining of Single-Class by Active Learning (MiSiCAL) paradigm is introduced where an AL policy is constructed through deep reinforcement learning and exploits quantity-accuracy correlations to build datasets on which high-performance models can be trained with regards to specific classes. MiSiCAL is especially helpful in the case of very large batch sizes since it does not require repeated model training sessions as is common in other AL methods. This is thanks to its ability to exploit fixed representations of the candidate data points. We find that MiSiCAL is able to outperform a random policy on 150 out of 171 COCO10k classes, while the strongest baseline only outperforms random on 101 classes.

**Keywords** Deep Q Learning, Image Segmentation, Reinforcement Learning, Class Imbalance

## 1 Introduction

Semantic segmentation refers to the task of labelling images in a pixel-wise fashion. Segmenting an image is often one of the first steps of image analysis and provides information about the nature and localization of the content of an image. High-performance image segmentation methods have enabled breakthroughs in fields as varied as autonomous driving,[1, 2] where it can complement LIDAR and RADAR data to produce semantic depth maps[3] and biomedical image segmentation[4] for surgery planning and diagnosis.[5] In the task of brain tumour segmentation on the BRATS dataset,[6] the application of deep learning methods led to dramatic improvements from 2012[7] as convolutional neural networks (CNN) overtook random forest models in popularity in 2015.

Recently, transformer-based architectures have achieved state-of-the-art performance both on popular semantic segmentation benchmarks[8, 9] and medical images[10]. CNN-Transformer hybrids, in particular, have also been used in the context of data scarce medical settings.[11, 12] Original Vision Transformers perform best when applied to large datasets and actually underperform CNNs on smaller datasets, likely due to the inductive biases inherent to CNNs helping in the scarce data regime at the cost of reduced flexibility and performance in large data settings.[13] In contrast to early image segmentation methods, for example based on colour clustering or thresholding,[14] which relied on very few parameters, modern deep-learning models often possess millions of parameters requiring training on large labelled training datasets to achieve their full potential.

While the amount of unlabelled data points available to a practitioner can be very large, acquiring labels for these data points is typically a long, tedious and expensive process. In the particular case of medical images, expert annotators are often required, further complicating the labelling task. Larger datasets usually result in lower model losses and greater performance,[15] yet in practice, one is often limited by a labelling budget, and it is often not feasible to label all available data points. Determining a policy to select points that will lead to the highest model performance for a fixed labelling budget is the crux of the active learning (AL) paradigm. Pretraining models on self-supervised pretext

tasks[16, 17] and thus leveraging unlabelled data can improve a model performance for a fixed labelling budget, yet labelled data are often required to fine-tune the pretrained model and reach optimal performance.[18]

In theory, selecting points at random is likely to be a suboptimal policy as not all points are expected to be equally informative.[19] Paradoxically, the random policy is nonetheless a very strong baseline in practice, especially for academic datasets.[20, 21] Several query policies have been developed leveraging model uncertainty such as entropy sampling and Bayesian Active Learning by Disagreement (BALD).[22, 23, 24, 25] in classification tasks, the *coreset* method attempts to select class diverse samples,[26] while the batchBALD method also promotes diversity within selected BALD batches by taking into account the mutual information between the samples.[27] Another class of policies aim to select unknown samples for labelling based on their expected impact on the model considered. These methods include the Expected Model Change Maximization (EMCM),[28] or the Influence Selection for Active Learning (ISAL).[29]

Active Learning on Large Language Models (LLMs) such as BERT is very computationally intensive.[30] This means large batch sizes have to be used and resources consumed to perform the training. In addition, there will be a wait time for the annotator in between labelling steps while the model trains which can be itself an issue.[31] Full training at each iteration is also impractical for pretrained large language models.[32] Therefore in practice, AL in the LLMs context is limited to fine-tuning operations of a few epochs on small models.[33]

Modern approaches include adversarial methods such as Variational Adversarial Active Learning (VAAL),[34] and Discriminative Active Learning (DAL).[35] Both VAAL and DAL train a binary classifier on the samples representations in the latent space of a variational autoencoder in the case of VAAL, or on the samples features as extracted by a relevant model such as a CNN in the case of image classification tasks for DAL. As such, neither VAAL nor DAL require repeated training of a model other than their discriminator, which itself can be very lightweight, nor explicit labelling (beyond marking a sample as “labelled”) and therefore have been shown to work well in large batch sizes. Another interesting work filters sample candidates on their predicted Shapley values before selecting the most promising based using the *coreset* method.[36] Since the data point Shapley value with regard to the task and model cannot be known before it is labelled, the authors trained a Shapley value predictor on known data points.

While both VAAL and DAL partially circumvent retraining a model from scratch and instead train lightweight classifiers on learnt latent representations of their input data to guide the new sample acquisition process, updating the models able to provide the latent representations of their original data can still be computationally expensive and might even prove prohibitive in the case of state-of-the-art large language models (LLMs). In addition, it is not obvious how these methods could be adapted to build a dataset enriched in specific classes using a binary classifier, since it might be hard to disentangle the representations from labelled and unlabelled samples from a single class from those of the other classes. Improving the performance metrics with regard to a single class is often crucial as they might be bottlenecks hard to optimise through general, class-agnostic AL frameworks.

Reinforcement learning based methods leverage features from other active learning frameworks such as uncertainty and diversity sampling as inputs to a Deep Q-Network (DQN) aiming to directly optimize the model performance based on the sample selection policy.[37, 38] Using reinforcement learning (RL) to directly learn an active learning policy—“learning how to learn”—was introduced in the NLP literature and showed great promise.[39] Such learned policies have been deployed in active learning settings with humans in the loop for person re-ID[40] and led to groundbreaking works in the case of ChatGPT, a large language model based on InstructGPT.[41] During the training of InstructGPT, humans ranked up to 9 model outputs based on sample prompts to train a reward model that is then used to fine-tune GPT-type models to produce human-likeable outputs through a Proximal Policy Optimization (PPO) algorithm.

Although the reward model is not used in a context of active learning in the InstructGPT paper, it highlights the importance of obtaining timely rewards during an iterative optimization process. In the original implementation of BALD, for example, it is recommended to train a new model from scratch after each batch selected during the active learning loop,[22] which is often impractical. While this is generally wasteful, it becomes unfeasible for large models and datasets. In addition, as models and datasets become large, the marginal impact of a single data point becomes small, and it becomes difficult to evaluate the individual contribution of newly added data points.[42]

In reinforcement learning, rewards can be provided at the end of a training episode to account for all the actions taken up to the end of the episode. Aside from leading to reward sparsification, which is generally considered undesirable in RL tasks,[43] it does not translate well to the active learning field since there only is one “episode” in the sense that each image can only be labelled once. Indeed, labelling the same data points several times and “forgetting” them from one episode to the next would lead to information leakage through the weights of the policy network and bias the active learning procedure. A high convergence rate of the active learning selection policy is crucial since every sample picked to improve the policy depletes the labelling budget. Sample efficiency is therefore important to successfully apply RL to

active learning, and Deep Q Networks are known to possess high sample efficiency thanks to their replay buffer coming in multiple flavours.[44, 45]

Here, we leverage RL methods in the context of active learning to select image patches from the COCO10k<sup>1</sup> [46] dataset under the CC BY 4.0 licence. The image patches are selected by a DQN based on the features obtained from a pretrained segmentation model to optimise the accuracy of that segmentation model on individual classes. The segmentation model is not retrained nor fine-tuned in between selection events and only the DQN weights are updated based on the ground-truth semantic content of the patches selected. This active learning paradigm is exceptionally lightweight as the target model (here the semantic segmentation model) is not retrained at each AL step, saving both training time but also the time necessary to update the candidate data point features. The use of an RL framework also helps seamlessly blend uncertainty and diversity in a single method, thereby bridging two popular AL paradigms without the need to manually tune the importance of each aspect. We envision this AL method might be extended to other classes of large deep learning models, such as LLMs, which are impractical to retrain and therefore ill-suited to traditional AL methods.

In contrast to most existing AL methods, the Mining of Single-Class by Active Learning (MiSiCAL), enables the selection of datapoints from chosen classes instead of from all classes. This will be particularly useful in the detection of outliers or out-of-distribution samples which by definition belong to underrepresented classes and on which performance metrics are difficult to improve.[47]

## 2 Background

### 2.1 Active learning

The remit of AL is to provide policies to pick the most informative samples from a pool of unlabelled data for which to query a label from an oracle or a user. The objective is often to train models effectively using as few data labels as possible, which is especially relevant when acquiring labels is expensive, such as in medical settings. Active Learning policies can be broadly divided between methods that use metrics computed directly with the model meant to be used on the target task and those that don't. DAL and VAAL belong to the latter category while uncertainty sampling, ISAL and EMCM belong to the former. The *coreset* method is perhaps the most popular diversity-based sampling method.[26] It attempts to locate a set of samples  $s^1$  with  $i$  samples under a constrained annotation budget  $b$  that will minimize the maximum distance between the chosen samples and the other  $j$  samples in the dataset, that is:

$$\min_{s^1: |s^1| \leq b} \max_i \min_{j \in s^1 \cup s^0} \Delta(\mathbf{x}_i, \mathbf{x}_j), \quad (1)$$

with  $s^0$  selected at random initially. The distance metric  $\Delta(\cdot, \cdot)$  is usually the Euclidean distance between the samples representations in the model's latent space. The success of the *coreset* method highlights that using compressed representations of high-dimensional inputs such as images as building blocks for AL heuristics can be very powerful. Seemingly simple pixel class histograms have still been shown to be powerful representations.[38] Uncertainty-based methods such as BALD and entropy are often used as benchmarks due to their robustness, ease of implementation and, in the limit of small batch sizes, very strong performances. The Shannon entropy[48] of the output of a classification problem with  $c$  classes given a training set  $D_{\text{train}}$  can be written as:[22]

$$\mathbb{H}[y = c | \mathbf{x}, D_{\text{train}}] = - \sum_c p(y = c | \mathbf{x}, D_{\text{train}}) \log p(y = c | \mathbf{x}, D_{\text{train}}), \quad (2)$$

while BALD can be computed as:

$$\mathbb{I}[y, \boldsymbol{\omega} | \mathbf{x}, D_{\text{train}}] = \mathbb{H}[y | \mathbf{x}, D_{\text{train}}] - \mathbb{E}_{p(\boldsymbol{\omega} | D_{\text{train}})} [\mathbb{H}[y | \mathbf{x}, \boldsymbol{\omega}]], \quad (3)$$

where  $\boldsymbol{\omega}$  is the model parameters. With a distribution in model weights, BALD attempts to select samples for which the average prediction is uncertain but resulting from the average of highly certain predictions. These points are expected to maximise the mutual information between the predictions and the model posterior. Obtaining a weight distribution can be done by Monte Carlo sampling  $T$  times dropout layers in a deep neural network, where BALD becomes ( $p_c^t = p(y = c | \mathbf{x}, D_{\text{train}})$  for the  $t^{\text{th}}$  sampling of  $\boldsymbol{\omega}$ ):

$$\mathbb{I}[y, \boldsymbol{\omega} | \mathbf{x}, D_{\text{train}}] = - \sum_c \left( \frac{1}{T} \sum_t p_c^t \right) \log \left( \frac{1}{T} \sum_t p_c^t \right) + \frac{1}{T} \sum_{c,t} p_c^t \log p_c^t. \quad (4)$$

As entropy and BALD information is computed at the pixel level for the output of segmentation models, they may be pooled at the image or patch level to further reduce their dimensionality. Both BALD information and a compressed

<sup>1</sup><https://creativecommons.org/licenses/by/4.0/legalcode>

representation of an image sample, such as its latent representation or its predicted pixel class histogram are powerful features by themselves. It is not always obvious how much weight to give to each one to ensure the best samples are picked. Passing this information as an observation to an agent following a reinforcement learning algorithm can sidestep this issue and allow the agent to find the proper weighting maximising the rewards it is receiving.

## 2.2 Q-learning

An agent attempts to maximise the expected return it obtains over the long run, with the return  $G_t$  expressed as the sum of future rewards  $R_t$ , discounted by a factor  $\gamma$  as:[49]

$$G_t = R_t + \gamma R_{t+1} + \gamma^2 R_{t+2} + \gamma^3 R_{t+3} + \dots = \sum_{k=0}^{\infty} \gamma^k R_{t+k}. \quad (5)$$

The return  $G_t$  can be defined recursively by noting that the sum of future expected rewards from step  $t + 1$  is  $G_{t+1}$ .

$$G_t = R_t + \gamma R_{t+1} + \gamma^2 R_{t+2} + \gamma^3 R_{t+3} + \dots, \quad (6)$$

$$= R_t + \gamma(R_{t+1} + \gamma R_{t+2} + \gamma^2 R_{t+3} + \dots), \quad (7)$$

$$= R_t + \gamma G_{t+1}. \quad (8)$$

In the context of a Markovian Decision process (MDP), the value function  $v_\pi(s)$  of a state  $s$  following a policy  $\pi$  is defined as the expected return when starting from the state  $s$  and following  $\pi$  afterwards.

$$v_\pi(s) \doteq \mathbb{E}_\pi[G_t | S_t = s] = \mathbb{E}_\pi \left[ \sum_{k=0}^{\infty} \gamma^k R_{t+k} \middle| S_t = s \right], \quad (9)$$

and similarly, the action-value function  $q_\pi(s, a)$  associated with taking action  $a$  in state  $s$  following  $\pi$  is written:

$$q_\pi(s, a) \doteq \mathbb{E}_\pi[G_t | S_t = s, A_t = a] = \mathbb{E}_\pi \left[ \sum_{k=0}^{\infty} \gamma^k R_{t+k} \middle| S_t = s, A_t = a \right], \quad (10)$$

A policy having an expected return superior or equal to all other policies for all states is referred to as an optimal policy. The optimal value function  $v_*(s)$  and action-value function  $q_*(s, a)$  are described by the following Bellman optimality equations, leveraging recursion from (8):

$$v_*(s) = \max_a \mathbb{E}_\pi \left[ R_t + \gamma v_*(S_{t+1}) \middle| S_t = s, A_t = a \right], \quad (11)$$

$$q_*(s, a) = \mathbb{E}_\pi \left[ R_t + \gamma \max_{a'} q_*(S_{t+1}, a') \middle| S_t = s, A_t = a \right]. \quad (12)$$

Equations (11) and (12) highlight that the value and action-value functions at a given position in the MDP can be entirely described in terms of the immediate reward received and the respective function value at the next step. The functions  $v_*(s)$  and  $q_*(s, a)$  are unknown, and they are usually estimated iteratively until convergence. The Temporal Difference method provides a simple way to update current estimates  $V(s)$  for a value function  $v_\pi(s)$  with a step size  $\alpha$  as:

$$V(S_t) \leftarrow V(S_t) + \alpha \underbrace{\left[ \underbrace{R_t + \gamma V(S_{t+1})}_{\text{TD target}} - V(S_t) \right]}_{\text{TD error}}. \quad (13)$$

This update is called TD(0) as the update uses only the current reward instead of a taking into account future discounted rewards. The TD method is bootstrapping as it is building an estimate upon a later estimate. The TD target shown in (13) is the most recent estimate of  $V(S_t)$  and both converge towards the optimal state-value function over subsequent updates.

As an off-policy TD variation for control, the Q-learning builds estimates for the action-value function  $q_\pi$  independently of the policy followed and is formulated as:

$$Q(S_t, A_t) \leftarrow Q(S_t, A_t) + \alpha \underbrace{\left[ \underbrace{R_t + \gamma \max_a Q(S_{t+1}, a)}_{\text{TD target}} - Q(S_t, A_t) \right]}_{\text{TD error}} \quad (14)$$

Approximating Q by a neural network forms the basic idea behind the original DQN implementation.

### 3 Method

#### 3.1 Overview

Here we introduce the MiSiCAL paradigm where a semantic segmentation model is not trained between active sample selection events and its fixed sample representations are leveraged by a RL-powered search procedure to acquire samples of a chosen specific class. This is in contrast to popular AL policies such as entropy or BALD which rely on successive training steps, at considerable computational costs, to acquire promising samples. MiSiCAL follows the philosophy of modern methods such as DAL and VAAL which acquire samples in a discriminative fashion based on fixed sample representations with a lightweight classifier.

MiSiCAL relies on the heuristic that increasing the representation of a specific class in a training dataset is likely to improve the performance of a model trained on this enriched dataset for metrics associated with the enriched class. MiSiCAL exploits the features of a pretrained segmentation model to optimise the acquisition of image patches from the COCO10k set with the objective of improving the performance of a semantic segmentation model on the IoU metric of a single class. This is unusual as other AL policies generally attempt to optimise the model performance over all classes simultaneously.

The optimization procedure is outlined in Figure. 1. A subset of patches  $D_{L,init}$  corresponding to 2.5% of COCO10k is randomly selected, and a semantic segmentation model is trained on it. This trained segmentation model is used to compute BALD features and class histograms for the remaining 624k patches of COCO10k (see section 3.2). Patch selection and DQN updates are alternated until the annotation budget is reached, in this case 5% of the COCO10k dataset.

To start the patch selection process as effectively as possible, a Double Deep Q-Network (DDQN)[50] is first trained for 4 epochs on  $D_{L,init}$  as shown in red squares on Figure. 2 where we show a representative plot for the SKATEBOARD class. At the end of each pretraining epoch and going through  $D_{L,init}$  patches, the active learning procedure is restarted from scratch while the weights and replay buffer of the DDQN are repeatedly updated. During the later epochs of the pretraining, the agent quickly acquires all SKATEBOARD containing patches then is left to select patches without SKATEBOARD pixels. The agent is then left to explore  $D_U$  with  $D_L$  starting at  $D_{L,init}$  and the DDQN weights copied from the last pretraining step, as shown in blue triangles. In contrast to the pretraining stage, the number of patches selected does not saturate as there are many SKATEBOARD images in  $D_U$  and the agent is not running out of candidates.

One can notice that the patch acquisition curve follows an exponential before plateauing rather than a step function even after training the DDQN in the pretraining phase. If the policy was fully greedy and had access to all samples from the start to pick from, it is likely that a step function would be observed. However, not only does the agent pick actions randomly with a probability  $\epsilon$  but when following the policy, it picks only the top patches from a randomly selected subset which can contain only a limited number of relevant patches.

#### 3.2 Implementation details

**Image preprocessing** All images are resized to squares of  $512^2$  pixels with the largest dimension resized to 512 pixels while the smallest dimension was padded with black to reach 512 pixels. Patches measure  $64^2$  pixels unless stated otherwise. Labels are resized in the same format as images with the padded area assigned a label ignored in the loss function of the segmentation model. Pixel values were scaled to the [0-1] range then normalized using a mean and standard deviation of respectively (0.485, 0.456, 0.406) and (0.229, 0.224, 0.225). Training images come from the COCO10k dataset while testing images are the 5k validation images from COCO164k. COCO10k is therefore divided into 640k patches of  $64^2$  pixels as 10k images are resized to sizes of  $512^2$  then cut into 64  $64^2$  pixels patches.  $D_{L,init}$  contains 2.5% of COCO10k or 16k patches.

To test and compute the action features at inference time, no augmentation is applied. During training, the following augmentation methods were used:

- Random scaling using scaling factors of 0.5, 0.75, 1.0, 1.25, 1.5
- Random crop and padding to  $512^2$  pixels.
- Random horizontal flip with a probability of 0.5
- Either a RandomAutocontrast or a RandomEqualize transform as implemented by torchvision.[51]

Importantly, all inference is performed on full images and the subdivision into patches is only performed later on the output pixel probabilities. Running the inference on the individual patches directly prevents the segmentation model from using the patch context and results in dramatic reduction in accuracy as indicated in Figure. 3a.

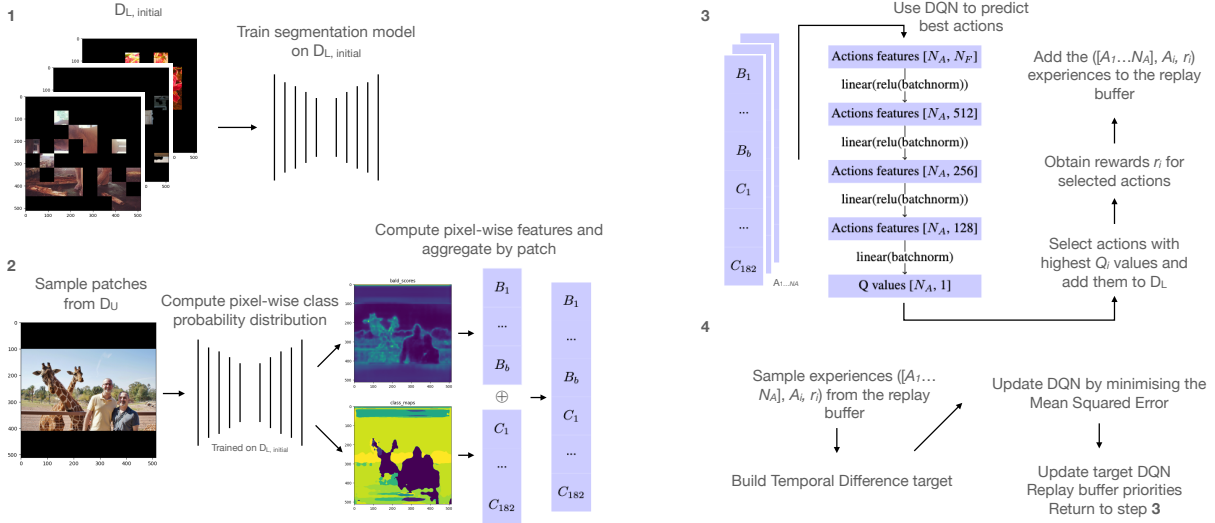


Figure 1: In **1**, an initial dataset  $D_{L,init}$  is used to train a segmentation model. **2** Calculation of the action features. An input image is resized, colour normalized, padded and its pixel wise class probability distribution  $p(y_i|x_i)$  is calculated via the segmentation model trained on  $D_{L,init}$ . The  $p(y_i|x_i)$  distribution is used to extract a pixel-wise BALD map. The map is then downsampled to the patch level using min, max and average pooling. Finally, a categorical vector is obtained from the segmented mask indicating whether a class is present in the patch. Both BALD and class features are then concatenated to produce the action features. As the segmentation model is not updated these action features are computed only once and kept fixed for the entire RL optimization procedure. In **3**, the DQN is used to compute the Q values of a sample of  $N_A$  from which the top-ranked are added to  $D_L$ , the corresponding rewards are computed and the experience tuples are added to the replay buffer. Finally, in **4**, the DQN is updated using experiences sampled from the multistep prioritized experience replay through (20) and (21). The target DQN is then updated as well in (18) along with the priorities of the replay buffer. A new action selection step is then performed in step **3**. Step **3** and **4** are repeated until a desired number of actions have been selected.

As shown in Figure. 3a, it is interesting to see that cutting large COCO164k images which are frequently 400-600 pixels wide in small patches of  $128^2$  pixels results in a dramatic loss in accuracy if patches are processed by themselves. Adding adjacent pixels, without their labels, to small patches can alleviate the accuracy drop (see Figure. 3b). Images are augmented according to the procedure described in 3.2. Test images are a selection of 2,000 COCO164k validation images and are resized to the same size as the training images. The images are used whole and not cut into patches. All runs are trained for a maximum of 50 epochs with a cosine annealing learning rate schedule with a 50 epochs period and starting at 0.001 with a minimum of 0. An early stopping criterion of the all class Mean IoU with patience of 5 epochs. Training and test images are cut into patches with a border made of pixels from the surrounding image to provide additional context. The border pixels are ignored during the loss computation but indirectly contribute to the training due to their presence in the convolution operations. All patches from training images with their borders are resized to  $321^2$  pixels prior to training while testing images are also resized to  $321^2$  pixels but not cut in patches. Error bars are the standard deviation of 5 seeds. The image size itself has a large influence on the Mean IoU achievable on test images of the same size as shown in Fig. A5. Indeed larger images may be necessary to resolve small objects and contribute reach high accuracies on the corresponding classes.

**Action representation** The actions corresponding to individual patches are computed as shown in Figure. 1(2). The first part of the feature vector consists of the maximum, minimum and mean of the BALD values  $\mathbf{B}$  of all  $k$  pixels contained in the patch  $\mathbf{x}$  considered as computed using (4).

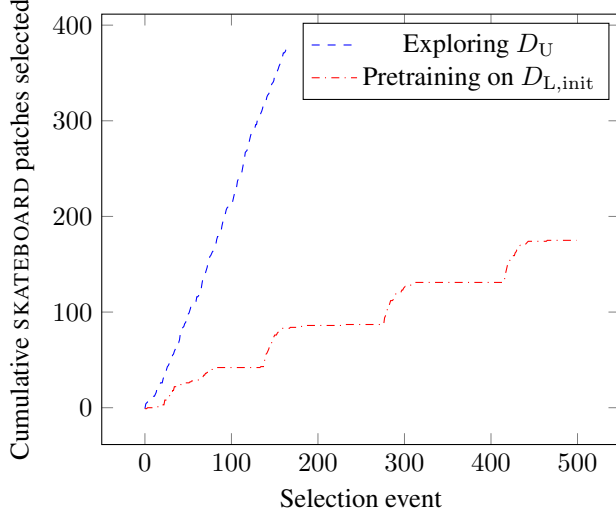


Figure 2: The DDQN pretraining phase of an active learning loop aiming to acquire patches containing SKATEBOARD pixels (an example class) is shown in red squares as the agent goes 4 times through  $D_{L,init}$  and becomes increasingly proficient at picking patches containing SKATEBOARD pixels. After the pretraining, the agent quickly acquires more SKATEBOARD pixels from  $D_U$ .

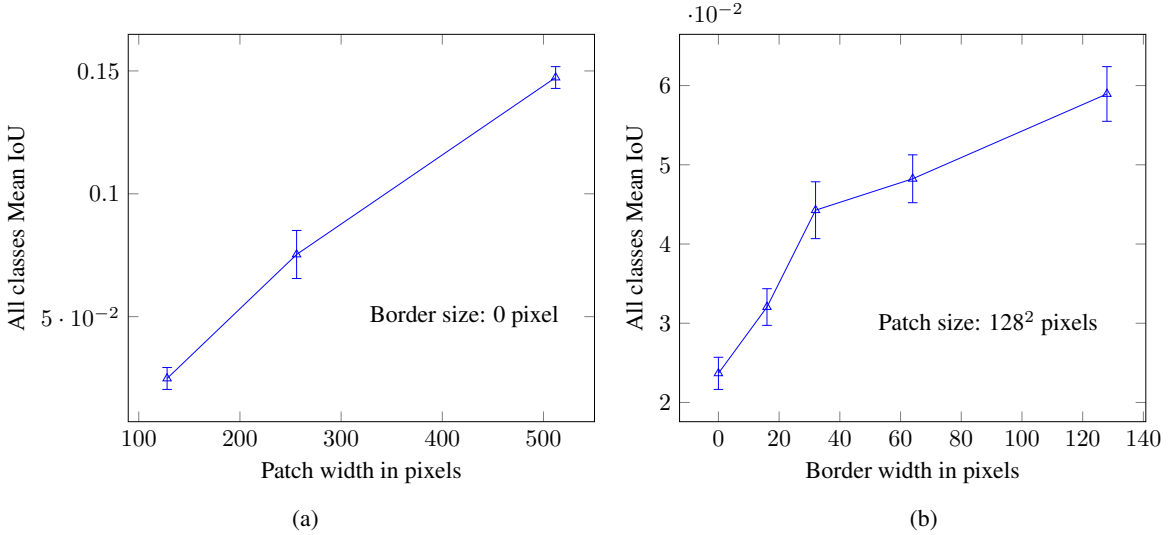


Figure 3: Evolution of the accuracy of the segmentation model with regard to the patch size and patch border for a sample of 2,000 images from the COCO164k training dataset.

$$\mathbf{F}_B = \begin{cases} B_0 & : \max(\mathbf{B}), \\ B_1 & : \min(\mathbf{B}), \\ B_2 & : \text{mean}(\mathbf{B}). \end{cases} \quad (15)$$

The class feature vector is a categorical vector where the index  $i$  corresponding to class  $c_i$  is 1 if the segmentation model predicts at least one pixel belonging to class  $c_i$  in the patch and 0 otherwise. With  $p_k(y = c_i | \mathbf{x})$  representing the probability of pixel  $k$ , part of patch  $\mathbf{x}$  to belong to class  $c_i$ , one can write the class feature vector  $\mathbf{F}_{c_i}$  as:

$$\mathbf{F}_{c_i} = 0 \quad \text{if} \quad \left[ \max_c p_k(y = c | \mathbf{x}) \neq p_k(y = c_i | \mathbf{x}) \quad \forall \quad k \right] \quad \text{else} \quad 1. \quad (16)$$

Eventually the action feature vector is obtained by concatenating the BALD and class feature vectors:

$$\mathbf{F} = \mathbf{F}_B \oplus \mathbf{F}_{c_i}. \quad (17)$$

**Reward** Once a patch has been selected, a reward is granted based on the semantic content of the ground truth segmentation mask corresponding to that patch. The reward is 1 if the patch contains at least a pixel from the class being optimized for and 0 otherwise. Using the change in the class IoU ( $\Delta$  IoU) after training for one epoch on the updated  $D_L$  after the addition of the selected samples didn't lead to a strong performance as shown in Fig. A10. This is presumably because rewards cannot be assigned at the patch level but need can only be obtained for the whole batch of selected samples therefore providing more "diluted" information through the rewards.

**Deep Q-networks** The Q-values are approximated by Deep Q-learning, the DDQN[50] flavour is used where the target network's weights  $\theta_{\text{target}}$  are updated at each local Q-network training batch with the local weights  $\theta_{\text{local}}$  using a soft update of the form:[52]

$$\theta_{\text{target}} = (1 - \beta)\theta_{\text{target}} + \beta\theta_{\text{local}}, \quad (18)$$

with  $\beta$  set to 0.002. This helps avoid Q-values overestimations and instabilities known to complicate the application of the DQN method as shown in Fig. A7.

The local network is updated using a Bellman equation,[53] very similar to (14) with the important difference that there is no explicit state considered. Indeed, as there is no model update, the model state does not change. Alternative state representations using the semantic content of  $D_L$  were attempted but did not lead to dramatic improvements. The DDQN update equation with learning rate  $\alpha$  is adapted from (2.2) with the difference that actions are selected with two networks with identical structures but different weights. The local network selects actions while the target network provides their Q-values estimates:

$$Q_{t+1}^{\text{local}}(S_t, A_t) = Q_t^{\text{local}}(S_t, A_t) + \alpha \left[ \underbrace{R_t + \gamma Q_t^{\text{target}} \left( S_t, \max_a Q_t^{\text{local}}(S_{t+1}, a) \right)}_{\text{TD target}} - Q_t^{\text{local}}(S_t, A_t) \right]. \quad (19)$$

In the DDQN case, the TD target is:

$$\text{TD target} = R_t + \gamma Q_t^{\text{target}} \left( S_t, \max_a Q_t^{\text{local}}(S_{t+1}, A_t) \right), \quad (20)$$

while the DDQN attempts to minimize the difference between the current Q-values and their TD targets using the mean squared error loss:

$$\text{MSE Loss} = \left( \text{TD target} - Q_t^{\text{local}}(S_t, A_t) \right)^2. \quad (21)$$

Indeed, the MSE Loss tends towards zero as the Q-values converge towards the optimal  $q_*(s, a)$  action-value function from (12).

**Deep Q-networks hyperparameters** The rate of soft update  $\beta$  is set to 0.002, setting  $\beta$  to higher values leads to faster convergence of the  $\theta_{\text{target}}$  with  $\theta_{\text{local}}$  and ultimately leads to instabilities with Q-values reaching very high ranges, which is an issue that the DDQN architecture is meant to avoid. On the other hand, setting  $\beta$  too low slows down the training as  $\theta_{\text{target}}$  become more insensitive to the ongoing training of the local DQN. DDQN behaviours with both high and low  $\beta$  values are shown in Fig. A7. Periodically copying the weights  $\theta_{\text{local}}$  to  $\theta_{\text{target}}$  prevents the Q-values from diverging but leads to small scale instabilities which prevents the DDQN losses from converging towards very low values. Gradients are clipped to 0.01 in an attempt to help and avoid instabilities though it appears that the expected stabilisation is tiny at best as shown in Fig. A9.

The network is trained with RMSProp with a learning rate of  $1 \times 10^{-3}$ , a weight decay of  $1 \times 10^{-4}$  and a batch size of 256 experiences. The agent follows an  $\epsilon$ -greedy policy with a constant  $\epsilon$  value of 0.05. Several schedules of  $\epsilon$ -annealing were explored in Fig. A8 with longer  $\epsilon$ -annealing generally performing better. Half of the total labelling budget (2.5% of  $D_U$ ) is picked at random in  $D_{L,\text{init}}$  and leveraged in pre-training, which corresponds to roughly the same amount of randomly picked samples as following a linear  $\epsilon$ -annealing over the selection of 5% of  $D_U$ .

At each sampling event, a Q value is computed for a randomly sampled subset of 2000 patches and the top 100 patches with the highest Q-values are selected. Several discount factors  $\gamma$  have been tried with the best results obtained for  $\gamma=0$ , which was used to obtain the results presented. Setting  $\gamma$  to values closer to 1, encourages exploration and leads to higher  $D_L$  entropies as shown in Fig. A6 but it seems that in the low data regime, focusing on short term rewards works best. In Fig. A10, one can see that  $\gamma = 0$  outperforms larger values in small batches, in particular when a longer  $\epsilon$ -annealing is applied.

**Buffer** To improve sample efficiency, many Q-learning methods use a replay buffer where experiences and rewards are stored to update the DQN at later stages instead of discarding them after a DQN update. When a replay buffer is present, experiences are sampled at every step from the buffer instead of only consisting of the last few experiences encountered by the agent. This helps the agent avoid “forgetting” about past experiences not recently encountered. A multistep buffer builds rewards as a discounted sum of rewards from previous steps and has been shown to lead to faster reward signal propagation and ultimately faster learning.[54]

The multistep buffer records current rewards as an  $n$ -step discounted accumulations of future rewards:

$$R_t^{(n)} = \sum_{k=0}^i \gamma^k R_{t+k} \quad (22)$$

The prioritized experience replay (PER)[55] component proved crucial to the effective training of the DDQN. The prioritized experience replay buffer assigns a higher weight to recent experiences and to experiences for which the MSE Loss was large. This enables the agent to spend more time learning on experiences for which its value function estimate was leading to a high loss. This is useful for sparse rewards which otherwise would contribute little to the DQN training. Instead of sampling the replay buffer uniformly, the PER samples an experience  $i$  with probability  $P(i)$  written:

$$P(i) = \frac{p_i^\eta}{\sum_k p_k^\eta}, \quad (23)$$

where  $\eta$  is an exponent modulating the scale of the importance sampling, reverting to uniform sampling for  $\eta = 0$ . The individual  $p_i$  can correspond to the TD error from (14) plus a small number to ensure a nonzero sampling probability for zero loss experiences. Alternatively  $p_i = \frac{1}{\text{rank}(i)}$  where  $\text{rank}(i)$  represents the rank of experience  $i$  when the replay buffer experiences are sorted by decreasing TD errors. The former is used in our case. As the experience replay introduces bias in the estimation of the expected values by changing the distribution of the stochastic updates in an uncontrolled fashion, one can correct for this bias using importance sampling weights  $w_i$ :

$$w_i = \left( \frac{1}{N} \cdot \frac{1}{P(i)} \right)^\zeta. \quad (24)$$

These weights multiply the TD error in the DQN update (after scaling by the maximum weight  $w_j$ ). When  $\zeta = 1$ , the non-uniform probabilities are fully compensated for. In practice  $\zeta$  is annealed from a starting value towards 1 which phases out the prioritization at the end of the training where unbiased estimators are required. The replay buffer has a capacity of  $1 \times 10^5$  experiences. A multistep buffer[56] with prioritized experience replay is used with a step number of 3.

**Segmentation model** The segmentation model architecture is LRASSP[57] as implemented in Pytorch[58] and is optimized using RMSprop[59] with a  $1 \times 10^{-3}$  learning rate and a cosine annealing schedule with a period of 50 epochs, a weight decay of  $1 \times 10^{-4}$  and a momentum of 0.9. An unweighted cross entropy loss is used. LRASSP is a small model with 3.7M parameters which enables fast training and inference while still reaching useful accuracies. In the low data regime, it was also found that smaller models led to faster convergence. To enable the Monte-Carlo sampling of the model outputs, two dropout layers with a probability of 50%[27] were added to respectively the high- and low- features before the output classifier layer.

## 4 Results and Discussion

A sample of results can be seen in Table. 1 where MiSiCAL is shown to perform well for classes starting with a high IoU metric such as BEAR or HORSE. In addition, patches containing classes for which the model used to calculate the features performs poorly, such as SKIS and FORK, can be successfully acquired. This is likely due to strong correlations between classes that the DDQN is able to exploit. For example, there are around 3k images containing SKIS in the training dataset of COCO164k. In the majority of these images, SKIS come in patches with PERSON and SNOW classes. With the addition of the BALD features, it can be expected that the model is able to acquire SKIS containing patches even if the class feature vector contains very few SKIS labels. A full table can be found in the Appendix in Table. A1. The MiSiCAL method outperforms random in 150 out of 171 classes, BALD outperforms in 101 out of 171 classes while the entropy policy outperforms in 19 classes. MiSiCAL is outperformed by random in a single class (CLOUDS). MiSiCAL outperforms the other policies with statistical significance 65 times while BALD did so for a single class (SCISSORS) and neither random and entropy managed to outperform the other policies.

Table 1: Comparison table of the end accuracies of models trained on 5% of COCO10k for each class present in the dataset with the accuracies at  $D_{L,init}$  corresponding to 2.5% of COCO10k shown for reference. Models are initially trained on a  $D_{L,init}$  corresponding to 2.5% of the whole dataset then patches are acquired from  $D_U$  using features calculated from the models trained on  $D_{L,init}$  and added to  $D_L$  until 5% of COCO10k has been labelled. Intersection over Union figures are given in percentages plus or minus the standard deviation over 5 seeds. Outperformance against the other policies at 5% are marked with an \* and obtained using the Welch t-test for unequal variances with a p-value < 0.05 threshold. The largest mean accuracies are highlighted in bold.

| Class                     | Random 2.5% | Random 5%  | Entropy 5% | BALD 5%            | MiSiCAL 5%         |
|---------------------------|-------------|------------|------------|--------------------|--------------------|
| Accuracy/baseball bat IoU | 0.02±0.04   | 0.00 ±0.00 | 0.15 ±0.34 | 0.02 ±0.05         | <b>5.30 ±1.41*</b> |
| Accuracy/bear IoU         | 38.19±9.74  | 49.92±4.40 | 37.53±2.79 | 62.53±5.25         | <b>65.02±2.03</b>  |
| Accuracy/dog IoU          | 31.39±3.86  | 35.85±2.10 | 29.77±2.92 | 40.65±2.12         | <b>46.68±2.94*</b> |
| Accuracy/fork IoU         | 0.02±0.04   | 0.09 ±0.19 | 0.10 ±0.21 | 0.46 ±0.47         | <b>8.52 ±1.34*</b> |
| Accuracy/horse IoU        | 30.17±3.93  | 36.97±3.73 | 33.47±2.96 | 35.01±2.94         | <b>44.53±4.28*</b> |
| Accuracy/hot dog IoU      | 14.85±2.54  | 21.71±4.69 | 17.86±4.90 | 23.08±3.74         | <b>28.67±2.12*</b> |
| Accuracy/scissors IoU     | 4.13±5.10   | 13.34±2.74 | 7.08 ±5.32 | <b>24.25±5.72*</b> | 16.59±6.84         |
| Accuracy/skateboard IoU   | 3.34±1.97   | 6.22 ±1.88 | 4.93 ±2.53 | 7.52 ±3.71         | <b>16.23±1.24*</b> |
| Accuracy/skis IoU         | 1.11±1.07   | 1.77 ±1.42 | 0.91 ±0.92 | 0.30 ±0.56         | <b>10.98±3.10*</b> |

From a certain perspective, it is remarkable that selectively accumulating patches containing a target class and training on the acquired patches does improve the class-specific performance metric. Indeed, in the correlations from Figure. A2, increasing a class pixel counts is shown to improve a class-specific accuracy metric but in the context of pixels from other classes also being present. One could imagine a case where pixel from the BEAR class could improve the accuracy of a model on the DOG class at test time by reducing the model confusion. A model having been trained exclusively on DOG images might mistake BEAR for DOG as they are both furry mammals. It is assumed that the randomly acquired patches during the  $\epsilon$ -greedy selection process help alleviate this potential problem. In addition, it is known that features learnt from the majority classes can be sufficient to classify under-represented classes.[60]

**Comparison of MiSiCAL with other large batch size methods** Going from a  $D_{L,init}$  of 16k patches to 32k patches effectively means selecting the pixel equivalent of 250 full size images. batchBALD is a method building on BALD aiming to maximise the intra-batch mutual information and has been shown to be robust to large batch sizes.[27] However, the batch size considered here is very large at 16k compared to the maximum batch size of 40 considered in the paper, at which point batchBALD was showing signs of a degrading performance and was essentially on par with a standard BALD method with a batch size four times smaller.

**Patches** An early design choice made was to process images as patches rather than whole. This decision is not trivial as COCO10k image dimensions are in the range of a few hundreds of pixels and could be processed directly whole or resized. It has been reported however that labelling whole images at the pixel level was a suboptimal strategy compared with spreading the same pixel budget over a larger number of images.[61] Taking this reasoning to the extreme, it was shown that a handful of pixels per image was sufficient to reach accuracies comparable to those obtained with orders of magnitude more pixels annotations spent on wholesale image annotations.[62]

Interestingly, we found that annotating sparse regions within an image, such as in patches, was crucial in reaching those accuracies as simply cutting down the original size images into patches and processing them individually was performing poorly. Indeed, one can see in Figure. 3a that cutting an image into increasingly smaller patches and training a model on the individual patches leads to a quickly deteriorating model performance. However, adding a border to the patches containing additional unlabelled image pixels partially rescues the accuracy drop occurring due to using small patches as shown in Figure 3b. Intuitively, this highlights that context is critical in successfully classifying individual pixels, presumably as information from pixels far away bring additional contextual information through the successive convolution layers.

Beyond the improvements in model performance, we have also shown that performing active learning from image regions can dramatically outperform the same procedure when carried out on whole images. Figure. 4 reveals that BALD, Entropy and Random do not significantly differ when considering whole images, while dramatic changes appear when selecting the pixels by patches. Note that the entropy policy performs exceptionally poorly, the reason being that images are resized and padded to a constant size before being divided into patches. The black and unlabelled padded regions lead to high model uncertainty which show up as high entropy zones even though there is no semantic

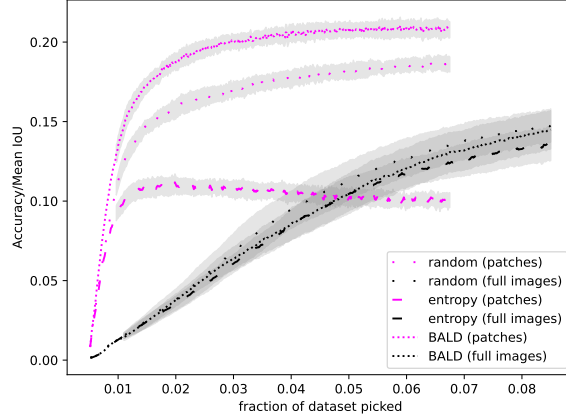


Figure 4: Comparison between actively selecting pixels to annotate by images or image patches for a fixed pixel annotation budget.

information in these patches. BALD does not suffer from this issue as the high average uncertainty arises from an average of uncertain predictions rather than an average of certain predictions. Although this could be alleviated by discarding patches containing a lot of padding, this issue might not be known a priori, so the poor performance of the entropy policy is left as is for fairness. The acquisition process is started with 50 full images randomly picked, and 2 additional images are selected from a randomly chosen subset of 2000 candidate images at each selection event. In the case of acquisition by patches, 3200 patches were randomly selected, and 100 patches were labelled out of a subset of 2000 patches randomly picked. Full images measure  $512^2$  pixels while patches measure  $64^2$  pixels. The accuracies were measured on the 5k images of the COCO164k test set. The LRASSP model is optimised using a batch size of 16, while the learning rate is  $1 \times 10^{-4}$  and the weight decay  $1 \times 10^{-4}$ . The model is trained for 1 epoch after each selection event and the shaded area correspond to the standard deviation of 5 seeds. The BALD policy is performed using 15 forward passes with the dropout layers enabled. The fraction of dataset picked is measured in terms of pixel counts.

**Heuristics for reward densification** A crucial ingredient of any RL method is the reward function. Since the Q-values are learnt from the rewards, the rewards are essentially the only inputs of the model aside from the hyperparameters, and the quality of the reward function can make or break a RL method.

Previous works aiming to use RL in active learning in the context of semantic segmentation directly used the segmentation model change in accuracy on a test set as new labels were added to  $D_L$ . [38, 63] Directly optimizing on the model accuracy is a very elegant approach as the end accuracy is the metric practitioners are actually interested in, as opposed to, for example, minimizing the model uncertainty. One issue is that the change in accuracy for the added labels does not scale well as the marginal contributions of the acquired samples becomes vanishingly small as  $D_L$  becomes very large. The model accuracy can also be noisy and dependent on the training parameters that were used. The change in class accuracy  $\Delta$  IoU was evaluated as a reward but did not lead to dramatic improvements as shown in Fig. A10. Rewards can also suffer from sparsity if the reward is provided after several selection steps or at the end of a selection episode.

In practical active learning settings, there is no concept of an episode as is customary in other RL contexts since data is only labelled once (assuming exact ground truths can be acquired), and it is therefore very important to quickly obtain a reliable reward signal, and avoid spending the labelling budget learning on suboptimal candidates. Reward shaping and densification aim to alleviate the issues associated with reward sparsity and help speed up the learning process. [64, 43]

Perhaps the simplest heuristic to improve a model accuracy in a classification task is to increase the representation of the target class in its training dataset. As shown in Figure. A1 when randomly selecting 5 image subsets of size (118000, 60000, 30000, 15000, 7500, 3750, 1875, 937, 468), or a total of 45 subsets, from the 118k images of the COCO164k training dataset and counting all pixels by class in each subset, it appears that the mean class IoU scales almost linearly with the logarithm of the pixel count. One can see that the pixel counts averaged by pixel bin in a class-agnostic way displays a broadly linear relationship with the class-agnostic average of IoUs in that bin. Trained on full images for 50 epochs using LRASSP and RMSProp with a  $1 \times 10^{-3}$  learning rate. The training was stopped when the mean IoU stopped improving for 5 epochs. The cross entropy loss is weighted with the inverse of the class frequency in the 118k COCO164k training dataset multiplied by the minimum non-zero class frequency in the same dataset.

Interestingly, the linear correlation broadly remains at the class level as can be seen in Figure. A2. Indeed, both well represented classes, such as AIRPLANE and underrepresented classes, such as BASEBALL BAT display a linear relationship between the  $\log_{10}(\text{pixel count})$  with the accuracy dropping very low below a 10k pixels threshold. It would be tempting to use the logarithm of the pixel counts as a proxy for the end IoU metric of the model simply based on the pixel histogram of  $D_L$ . With  $i$  the class indices,  $K_i$  a class specific scaling factor and  $h_i$  the pixel count of class  $i$  in  $D_L$ , one could estimate the Mean IoU metric associated with a training dataset as:

$$\text{Mean IoU} \approx \sum_i K_i \log(h_i). \quad (25)$$

In Figure. A4, a thought experiment for hypothetical datasets where the class IoUs indeed scale with the logarithm of the pixel count and all  $K_i$  factors are equal shows that for class imbalanced datasets, selecting samples that would be expected to maximise the predicted Mean IoU could strongly outperform the random sampling strategy. One can see that when the pixel distribution sampled is balanced, the gap between random sampling and sampling uniformly from all classes (which is expected to be a strong baseline to build a high mean IoU) is small. On the other hand, for larger class imbalances, the expected improvement from the random sampling is larger. As the training set of COCO164k possesses a non-negligible degree of class imbalance, picking samples based on the expected change in Mean IoU induced by their addition to  $D_L$  would be expected to strongly outperform the random sampling strategy. Unfortunately the class specific scaling coefficients  $K_i$  are not known a priori and this policy barely outperforms a random policy if equal  $K_i$  are assumed.

As shown in Figure. A3, while the relationship of  $\log_{10}(\text{pixel count})$  with class IoUs are broadly linear, the slope of these correlations have a wide distribution which does not correlate with the class frequency, making it hard to estimate. Assuming equal  $K_i$  did outperform the random strategy in our tests (not shown) but did not outperform BALD and therefore the focus was shifted from optimizing the model performance on the IoU metric to optimizing the IoU metric of specific classes. Interestingly, this distribution of  $K_i$  means that directly optimising the  $D_L$  pixel count histogram entropy did not outperform BALD. Very high pixel count histogram entropies can quickly be reached, but unfortunately this does not translate to very high Mean IoU metrics. In datasets with very strong class imbalances where a few classes dominate the pixel counts, such as CityScapes,[65] directly optimising the entropy of the  $D_L$  normalised pixel histograms might be a viable option.

When a single class is considered, accumulating pixels from that class can improve the IoU metric of that class. Both actions features and rewards are categorical as using normalized pixel histograms was found to weaken the signal from small objects such as knives and forks while using rewards linked to the amount of pixels acquired tended to favour picking large surfaces which might not have been informative or contained much context.

Since categorical annotations are used, where a vector simply contains whether a class is present or not in the patch, it makes the annotation process in real world settings more lightweight than if wholesale pixel annotations were required. This requirement is softer than most AL methods but more stringent than VAAL and DAL which only require to mark a sample as labelled without the actual need to label it straight away. Compared to VAAL and DAL which do not necessarily use features from a model specific task, MiSiCAL directly computes uncertainty metrics and representations from the task-specific model. Associated with an RL-powered algorithm able to take advantage of user defined rewards, the metrics can be leveraged online to reach complex objectives beyond the ability to predict whether a sample has been labelled or not irrespective of its semantic content.

**Shortcomings and limitations** The DQN powered procedure is not as easy to set up as the BALD or entropy policies and may require some hyperparameters tuning. The selection process is also dependent on the rewards function which rests on data biases which might be specific to COCO164k. For datasets containing duplicates or very similar images, there could be a risk of seeing the DQN select such images repeatedly to reap high rewards without actually leading to a high performance training dataset. This issue would be present if searching through highly redundant images such as those from a CCTV stream but would not be expected to be problematic for highly diverse sources such as those from histopathology slides or satellites images.

## 5 Conclusion

It is shown that Mining of Single-Class by Active Learning can serve as a lightweight paradigm to dramatically boost the performance of a semantic segmentation model on selected classes if convenient heuristics for data value can be found. For COCO10k, the logarithm of the pixel count from a single class in a training dataset was found to correlate with the IoU metric of segmentation model trained on the dataset. This opens new possibilities to use AL in the context

of model optimization which are too costly or impractical to repeatedly train to acquiring additional informative samples such as LLMs. The possibility to acquire samples from a single class and subsequently boost the accuracy of models trained with the new samples is also presented. Within the DDQN framework, a suitable weighting of model diversity and model uncertainty emerges to allow the agent to maximise the acquisition of relevant patches without the need to manually weight these contributions.

## References

- [1] Michael Trembl, José Arjona-Medina, Thomas Unterthiner, Rupesh Durgesh, Felix Friedmann, Peter Schuberth, Andreas Mayr, Martin Heusel, Markus Hofmarcher, Michael Widrich, et al. Speeding up semantic segmentation for autonomous driving. 2016.
- [2] Çağrı Kaymak and Ayşegül Uçar. A brief survey and an application of semantic image segmentation for autonomous driving. *Handbook of Deep Learning Applications*, pages 161–200, 2019.
- [3] Juergen Dickmann, Jens Klappstein, Markus Hahn, Nils Appenrodt, Hans-Ludwig Bloecher, Klaudius Werber, and Alfons Sailer. Automotive radar the key technology for autonomous driving: From detection and ranging to environmental understanding. In *2016 IEEE Radar Conference (RadarConf)*, pages 1–6. IEEE, 2016.
- [4] Olaf Ronneberger, Philipp Fischer, and Thomas Brox. U-net: Convolutional networks for biomedical image segmentation. In *International Conference on Medical image computing and computer-assisted intervention*, pages 234–241. Springer, 2015.
- [5] Xiao Xiao, Shen Lian, Zhiming Luo, and Shaozi Li. Weighted res-unet for high-quality retina vessel segmentation. In *2018 9th international conference on information technology in medicine and education (ITME)*, pages 327–331. IEEE, 2018.
- [6] Bjoern H Menze, Andras Jakab, Stefan Bauer, Jayashree Kalpathy-Cramer, Keyvan Farahani, Justin Kirby, Yuliya Burren, Nicole Porz, Johannes Slotboom, Roland Wiest, et al. The multimodal brain tumor image segmentation benchmark (brats). *IEEE transactions on medical imaging*, 34(10):1993–2024, 2014.
- [7] Mina Ghaffari, Arcot Sowmya, and Ruth Oliver. Automated brain tumor segmentation using multimodal brain scans: a survey based on models submitted to the brats 2012–2018 challenges. *IEEE reviews in biomedical engineering*, 13:156–168, 2019.
- [8] Zhe Chen, Yuchen Duan, Wenhai Wang, Junjun He, Tong Lu, Jifeng Dai, and Yu Qiao. Vision transformer adapter for dense predictions. *arXiv preprint arXiv:2205.08534*, 2022.
- [9] Wenhui Wang, Hangbo Bao, Li Dong, Johan Bjorck, Zhiliang Peng, Qiang Liu, Kriti Aggarwal, Owais Khan Mohammed, Saksham Singhal, Subhojit Som, et al. Image as a foreign language: Beit pretraining for all vision and vision-language tasks. *arXiv preprint arXiv:2208.10442*, 2022.
- [10] Jeya Maria Jose Valanarasu, Poojan Oza, Ilker Hacihaliloglu, and Vishal M Patel. Medical transformer: Gated axial-attention for medical image segmentation. In *International Conference on Medical Image Computing and Computer-Assisted Intervention*, pages 36–46. Springer, 2021.
- [11] Jieneng Chen, Yongyi Lu, Qihang Yu, Xiangde Luo, Ehsan Adeli, Yan Wang, Le Lu, Alan L Yuille, and Yuyin Zhou. Transunet: Transformers make strong encoders for medical image segmentation. *arXiv preprint arXiv:2102.04306*, 2021.
- [12] Yunhe Gao, Mu Zhou, and Dimitris N Metaxas. Utnet: a hybrid transformer architecture for medical image segmentation. In *International Conference on Medical Image Computing and Computer-Assisted Intervention*, pages 61–71. Springer, 2021.
- [13] Alexey Dosovitskiy, Lucas Beyer, Alexander Kolesnikov, Dirk Weissenborn, Xiaohua Zhai, Thomas Unterthiner, Mostafa Dehghani, Matthias Minderer, Georg Heigold, Sylvain Gelly, et al. An image is worth 16x16 words: Transformers for image recognition at scale. *arXiv preprint arXiv:2010.11929*, 2020.
- [14] Yu-Jin Zhang. An overview of image and video segmentation in the last 40 years. *Advances in Image and Video Segmentation*, pages 1–16, 2006.
- [15] Tom Henighan, Jared Kaplan, Mor Katz, Mark Chen, Christopher Hesse, Jacob Jackson, Heewoo Jun, Tom B Brown, Prafulla Dhariwal, Scott Gray, et al. Scaling laws for autoregressive generative modeling. *arXiv preprint arXiv:2010.14701*, 2020.
- [16] Xinlei Chen, Saining Xie, and Kaiming He. An empirical study of training self-supervised vision transformers. In *Proceedings of the IEEE/CVF International Conference on Computer Vision*, pages 9640–9649, 2021.

- [17] Mathilde Caron, Hugo Touvron, Ishan Misra, Hervé Jégou, Julien Mairal, Piotr Bojanowski, and Armand Joulin. Emerging properties in self-supervised vision transformers. In Proceedings of the IEEE/CVF international conference on computer vision, pages 9650–9660, 2021.
- [18] Yucheng Tang, Dong Yang, Wenqi Li, Holger R Roth, Bennett Landman, Daguang Xu, Vishwesh Nath, and Ali Hatamizadeh. Self-supervised pre-training of swin transformers for 3d medical image analysis. In Proceedings of the IEEE/CVF Conference on Computer Vision and Pattern Recognition, pages 20730–20740, 2022.
- [19] Sanjoy Dasgupta. Analysis of a greedy active learning strategy. Advances in neural information processing systems, 17, 2004.
- [20] Sudhanshu Mittal, Maxim Tatarchenko, Özgün Çiçek, and Thomas Brox. Parting with illusions about deep active learning. arXiv preprint arXiv:1912.05361, 2019.
- [21] Qiang Hu, Yuejun Guo, Maxime Cordy, Xiaofei Xie, Wei Ma, Mike Papadakis, and Yves Le Traon. Towards exploring the limitations of active learning: An empirical study. In 2021 36th IEEE/ACM International Conference on Automated Software Engineering (ASE), pages 917–929. IEEE, 2021.
- [22] Yarin Gal, Riashat Islam, and Zoubin Ghahramani. Deep bayesian active learning with image data. In International Conference on Machine Learning, pages 1183–1192. PMLR, 2017.
- [23] Neil Houlsby, Ferenc Huszár, Zoubin Ghahramani, and Máté Lengyel. Bayesian active learning for classification and preference learning. arXiv preprint arXiv:1112.5745, 2011.
- [24] Alex Holub, Pietro Perona, and Michael C Burl. Entropy-based active learning for object recognition. In 2008 IEEE Computer Society Conference on Computer Vision and Pattern Recognition Workshops, pages 1–8. IEEE, 2008.
- [25] Jordan T Ash, Chicheng Zhang, Akshay Krishnamurthy, John Langford, and Alekh Agarwal. Deep batch active learning by diverse, uncertain gradient lower bounds. arXiv preprint arXiv:1906.03671, 2019.
- [26] Ozan Sener and Silvio Savarese. Active learning for convolutional neural networks: A core-set approach. arXiv preprint arXiv:1708.00489, 2017.
- [27] Andreas Kirsch, Joost Van Amersfoort, and Yarin Gal. Batchbald: Efficient and diverse batch acquisition for deep bayesian active learning. Advances in neural information processing systems, 32, 2019.
- [28] Wenbin Cai, Ya Zhang, and Jun Zhou. Maximizing expected model change for active learning in regression. In 2013 IEEE 13th international conference on data mining, pages 51–60. IEEE, 2013.
- [29] Zhuoming Liu, Hao Ding, Huaping Zhong, Weijia Li, Jifeng Dai, and Conghui He. Influence selection for active learning. In Proceedings of the IEEE/CVF International Conference on Computer Vision, pages 9274–9283, 2021.
- [30] Liat Ein Dor, Alon Halfon, Ariel Gera, Eyal Shnarch, Lena Dankin, Leshem Choshen, Marina Danilevsky, Ranit Aharonov, Yoav Katz, and Noam Slonim. Active learning for bert: An empirical study. In Proceedings of the 2020 Conference on Empirical Methods in Natural Language Processing (EMNLP), pages 7949–7962, 2020.
- [31] Zhisong Zhang, Emma Strubell, and Eduard Hovy. A survey of active learning for natural language processing. arXiv preprint arXiv:2210.10109, 2022.
- [32] Katerina Margatina, Loïc Barrault, and Nikolaos Aletras. On the importance of effectively adapting pretrained language models for active learning. arXiv preprint arXiv:2104.08320, 2021.
- [33] Hannah Rose Kirk, Bertie Vidgen, and Scott A Hale. Is more data better? re-thinking the importance of efficiency in abusive language detection with transformers-based active learning. arXiv preprint arXiv:2209.10193, 2022.
- [34] Samarth Sinha, Sayna Ebrahimi, and Trevor Darrell. Variational adversarial active learning. In Proceedings of the IEEE/CVF International Conference on Computer Vision, pages 5972–5981, 2019.
- [35] Daniel Gissin and Shai Shalev-Shwartz. Discriminative active learning. arXiv preprint arXiv:1907.06347, 2019.
- [36] Amirata Ghorbani, James Zou, and Andre Esteva. Data shapley valuation for efficient batch active learning. arXiv preprint arXiv:2104.08312, 2021.
- [37] Emma Slade and Kim M Branson. Deep reinforced active learning for multi-class image classification. arXiv preprint arXiv:2206.13391, 2022.
- [38] Arantxa Casanova, Pedro O Pinheiro, Negar Rostamzadeh, and Christopher J Pal. Reinforced active learning for image segmentation. arXiv preprint arXiv:2002.06583, 2020.
- [39] Meng Fang, Yuan Li, and Trevor Cohn. Learning how to active learn: A deep reinforcement learning approach. arXiv preprint arXiv:1708.02383, 2017.

- [40] Zimo Liu, Jingya Wang, Shaogang Gong, Huchuan Lu, and Dacheng Tao. Deep reinforcement active learning for human-in-the-loop person re-identification. In Proceedings of the IEEE/CVF international conference on computer vision, pages 6122–6131, 2019.
- [41] Long Ouyang, Jeff Wu, Xu Jiang, Diogo Almeida, Carroll L. Wainwright, Pamela Mishkin, Chong Zhang, Sandhini Agarwal, Katarina Slama, Alex Ray, John Schulman, Jacob Hilton, Fraser Kelton, Luke Miller, Maddie Simens, Amanda Askell, Peter Welinder, Paul Christiano, Jan Leike, and Ryan Lowe. Training language models to follow instructions with human feedback, 2022.
- [42] Amirata Ghorbani and James Zou. Data shapley: Equitable valuation of data for machine learning. In International Conference on Machine Learning, pages 2242–2251. PMLR, 2019.
- [43] Farzan Memarian, Wonjoon Goo, Rudolf Lioutikov, Scott Niekum, and Ufuk Topcu. Self-supervised online reward shaping in sparse-reward environments. In 2021 IEEE/RSJ International Conference on Intelligent Robots and Systems (IROS), pages 2369–2375. IEEE, 2021.
- [44] William Fedus, Prajit Ramachandran, Rishabh Agarwal, Yoshua Bengio, Hugo Larochelle, Mark Rowland, and Will Dabney. Revisiting fundamentals of experience replay. In International Conference on Machine Learning, pages 3061–3071. PMLR, 2020.
- [45] Matteo Hessel, Joseph Modayil, Hado Van Hasselt, Tom Schaul, Georg Ostrovski, Will Dabney, Dan Horgan, Bilal Piot, Mohammad Azar, and David Silver. Rainbow: Combining improvements in deep reinforcement learning. In Thirty-second AAAI conference on artificial intelligence, 2018.
- [46] Holger Caesar, Jasper Uijlings, and Vittorio Ferrari. Coco-stuff: Thing and stuff classes in context. In Proceedings of the IEEE conference on computer vision and pattern recognition, pages 1209–1218, 2018.
- [47] Haseeb Ali, Mohd Najib Mohd Salleh, Rohmat Saedudin, Kashif Hussain, and Muhammad Faheem Mushtaq. Imbalance class problems in data mining: A review. Indonesian Journal of Electrical Engineering and Computer Science, 14(3):1560–1571, 2019.
- [48] Claude E Shannon. A mathematical theory of communication. The Bell system technical journal, 27(3):379–423, 1948.
- [49] Richard S Sutton and Andrew G Barto. Reinforcement learning: An introduction. MIT press, 2018.
- [50] Hado Van Hasselt, Arthur Guez, and David Silver. Deep reinforcement learning with double q-learning. In Proceedings of the AAAI conference on artificial intelligence, volume 30, 2016.
- [51] Daniel Falbel. torchvision: Models, Datasets and Transformations for Images, 2023. <https://torchvision.mlverse.org>, <https://github.com/mlverse/torchvision>.
- [52] Timothy P Lillicrap, Jonathan J Hunt, Alexander Pritzel, Nicolas Heess, Tom Erez, Yuval Tassa, David Silver, and Daan Wierstra. Continuous control with deep reinforcement learning. arXiv preprint arXiv:1509.02971, 2015.
- [53] Thomas G Dietterich. Hierarchical reinforcement learning with the maxq value function decomposition. Journal of artificial intelligence research, 13:227–303, 2000.
- [54] Lingheng Meng, Rob Gorbet, and Dana Kulić. The effect of multi-step methods on overestimation in deep reinforcement learning. In 2020 25th International Conference on Pattern Recognition (ICPR), pages 347–353. IEEE, 2021.
- [55] Tom Schaul, John Quan, Ioannis Antonoglou, and David Silver. Prioritized experience replay. arXiv preprint arXiv:1511.05952, 2015.
- [56] J Fernando Hernandez-Garcia and Richard S Sutton. Understanding multi-step deep reinforcement learning: a systematic study of the dqn target. arXiv preprint arXiv:1901.07510, 2019.
- [57] Andrew Howard, Mark Sandler, Grace Chu, Liang-Chieh Chen, Bo Chen, Mingxing Tan, Weijun Wang, Yukun Zhu, Ruoming Pang, Vijay Vasudevan, et al. Searching for mobilenetv3. In Proceedings of the IEEE/CVF international conference on computer vision, pages 1314–1324, 2019.
- [58] Adam Paszke, Sam Gross, Soumith Chintala, Gregory Chanan, Edward Yang, Zachary DeVito, Zeming Lin, Alban Desmaison, Luca Antiga, and Adam Lerer. Automatic differentiation in pytorch. 2017.
- [59] Geoffrey Hinton, Nitish Srivastava, and Kevin Swersky. Neural networks for machine learning lecture 6a overview of mini-batch gradient descent. Cited on, 14(8):2, 2012.
- [60] Michela Carlotta Massi, Francesca Gasperoni, Francesca Ieva, and Anna Maria Paganoni. Feature selection for imbalanced data with deep sparse autoencoders ensemble. Statistical Analysis and Data Mining: The ASA Data Science Journal, 15(3):376–395, 2022.

- [61] Bo Li and Tommy Sonne Alstrøm. On uncertainty estimation in active learning for image segmentation. arXiv preprint arXiv:2007.06364, 2020.
- [62] Gyungin Shin, Weidi Xie, and Samuel Albanie. All you need are a few pixels: semantic segmentation with pixelpick. In Proceedings of the IEEE/CVF International Conference on Computer Vision, pages 1687–1697, 2021.
- [63] Usman Ahmad Usmani, Junzo Watada, Jafreezal Jaafar, Izzatdin Abdul Aziz, and Arunava Roy. A reinforced active learning algorithm for semantic segmentation in complex imaging. IEEE Access, 9:168415–168432, 2021.
- [64] Abhishek Gupta, Aldo Pacchiano, Yuexiang Zhai, Sham M Kakade, and Sergey Levine. Unpacking reward shaping: Understanding the benefits of reward engineering on sample complexity. arXiv preprint arXiv:2210.09579, 2022.
- [65] Marius Cordts, Mohamed Omran, Sebastian Ramos, Timo Rehfeld, Markus Enzweiler, Rodrigo Benenson, Uwe Franke, Stefan Roth, and Bernt Schiele. The cityscapes dataset for semantic urban scene understanding. In Proceedings of the IEEE conference on computer vision and pattern recognition, pages 3213–3223, 2016.

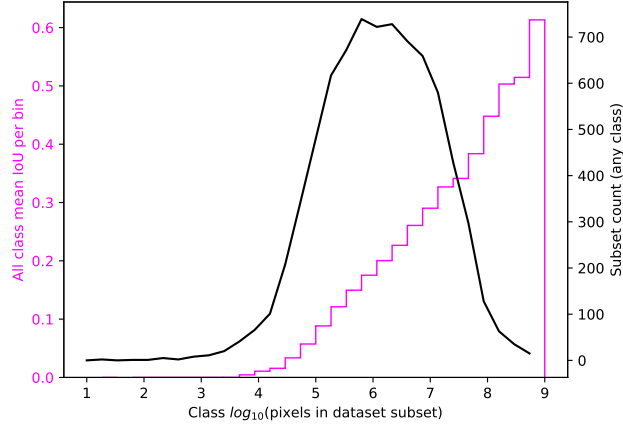


Figure A1: Class IoU binned and averaged by subset  $\log_{10}$  (pixel count) displays a stair-like behaviour in red with the y-axis on the left. The count of subset by class per bin is shown in green and displays a bell-shaped distribution with the y-axis displayed on the right.

## A Appendix

Table A1: Comparison table of the end accuracies of models trained on 5% of COCO10k for each class present in the dataset with the accuracies at  $D_{L,init}$  corresponding to 2.5% of COCO10k shown for reference. Models are initially trained on a  $D_{L,init}$  corresponding to 2.5% of the whole dataset then patches are acquired from  $D_U$  using features calculated from the models trained on  $D_{L,init}$  and added to  $D_L$  until 5% of COCO10k has been labelled. Intersection over Union figures are given in percentages plus or minus the standard deviation over 5 seeds. Outperformance against the other policies at 5% are marked with an \* and obtained using the Welch t-test for unequal variances with a p-value < 0.05 threshold. The largest mean accuracies are highlighted in bold.

| Class                       | Random 2.5% | Random 5%         | Entropy 5% | BALD 5%           | MiSiCAL 5%         |
|-----------------------------|-------------|-------------------|------------|-------------------|--------------------|
| Accuracy/airplane IoU       | 36.76±2.06  | 40.55±2.45        | 33.38±2.52 | 36.77±3.49        | <b>41.49±4.91</b>  |
| Accuracy/apple IoU          | 13.65±5.74  | 18.64±5.57        | 16.08±3.25 | 24.07±3.36        | <b>26.31±2.00</b>  |
| Accuracy/backpack IoU       | 1.47±1.38   | 1.97±1.61         | 1.24 ±1.11 | 3.73 ±1.97        | <b>4.79 ±1.47</b>  |
| Accuracy/banana IoU         | 31.41±1.63  | 34.75±2.75        | 29.24±2.02 | <b>36.67±1.76</b> | 36.36±4.03         |
| Accuracy/banner IoU         | 8.92±1.52   | <b>10.30±1.49</b> | 9.41 ±1.87 | 9.93 ±2.62        | 8.83 ±0.92         |
| Accuracy/baseball bat IoU   | 0.02±0.04   | 0.00 ±0.00        | 0.15 ±0.34 | 0.02 ±0.05        | <b>5.30 ±1.41*</b> |
| Accuracy/baseball glove IoU | 0.00±0.01   | 0.55 ±0.81        | 0.00 ±0.00 | 0.88 ±1.96        | <b>5.64 ±2.63*</b> |
| Accuracy/bear IoU           | 38.19±9.74  | 49.92±4.40        | 37.53±2.79 | 62.53±5.25        | <b>65.02±2.03</b>  |
| Accuracy/bed IoU            | 32.98±1.80  | 36.86±2.05        | 32.60±1.20 | 36.81±1.86        | <b>38.78±1.75</b>  |
| Accuracy/bench IoU          | 14.78±1.99  | 18.21±0.69        | 14.83±0.89 | 20.27±1.71        | <b>21.67±0.97</b>  |
| Accuracy/bicycle IoU        | 29.23±4.56  | 34.80±3.19        | 27.91±5.33 | 33.67±2.75        | <b>41.56±2.91*</b> |
| Accuracy/bird IoU           | 21.72±4.56  | 28.50±4.24        | 20.49±8.30 | 37.24±4.63        | <b>41.17±3.95</b>  |
| Accuracy/blanket IoU        | 0.55±0.75   | 0.79 ±0.55        | 1.02 ±0.23 | 0.84 ±0.41        | <b>2.37 ±1.55</b>  |
| Accuracy/boat IoU           | 27.63±2.32  | 28.86±0.82        | 25.09±2.65 | 29.87±0.62        | <b>31.84±1.87*</b> |
| Accuracy/book IoU           | 12.50±1.32  | 14.18±1.37        | 11.75±1.13 | 17.14±1.68        | <b>17.87±0.92</b>  |
| Accuracy/bottle IoU         | 9.91±3.03   | 12.76±2.48        | 10.59±3.67 | 16.54±1.78        | <b>19.19±1.45*</b> |
| Accuracy/bowl IoU           | 15.03±1.44  | 16.88±1.99        | 16.59±2.26 | 19.06±0.75        | <b>23.35±1.80*</b> |
| Accuracy/branch IoU         | 0.40±0.69   | 1.48 ±1.67        | 0.07 ±0.08 | 0.96 ±0.87        | <b>2.91 ±1.48</b>  |
| Accuracy/bridge IoU         | 4.55±3.34   | 5.06 ±1.45        | 3.55 ±1.54 | 6.15 ±3.37        | <b>9.80 ±3.15</b>  |
| Accuracy/broccoli IoU       | 26.37±5.11  | 29.75±5.39        | 33.15±3.99 | 35.22±1.97        | <b>36.71±2.79</b>  |
| Accuracy/building-other IoU | 37.66±0.94  | 38.98±0.69        | 36.71±0.90 | 38.49±0.70        | <b>39.04±0.55</b>  |
| Accuracy/bus IoU            | 45.84±0.49  | 50.04±2.31        | 44.76±2.87 | 45.70±3.17        | <b>57.93±1.56*</b> |
| Accuracy/bush IoU           | 10.51±2.17  | 11.16±3.96        | 10.22±2.28 | 8.49 ±0.94        | <b>14.78±1.78</b>  |
| Accuracy/cabinet IoU        | 7.71±2.25   | 9.19 ±1.33        | 11.30±1.95 | 11.31±2.34        | <b>12.49±3.80</b>  |
| Accuracy/cage IoU           | 0.17±0.26   | 0.84 ±0.73        | 0.47 ±0.57 | <b>3.55 ±0.89</b> | 3.41 ±1.47         |
| Accuracy/cake IoU           | 15.37±2.38  | 18.52±2.95        | 14.52±2.04 | <b>23.28±1.99</b> | 23.10±2.29         |

Continued on next page

Mining of Single-Class by Active Learning for Semantic Segmentation

| Class                        | Random 2.5% | Random 5%         | Entropy 5% | BALD 5%           | MiSiCAL 5%         |
|------------------------------|-------------|-------------------|------------|-------------------|--------------------|
| Accuracy/car IoU             | 25.84±3.89  | 30.37±2.44        | 28.65±1.21 | 31.33±1.28        | <b>35.81±2.00*</b> |
| Accuracy/cardboard IoU       | 1.82±2.40   | 4.61 ±2.56        | 1.15 ±1.09 | 5.05 ±2.37        | <b>8.26 ±1.31*</b> |
| Accuracy/carpet IoU          | 25.63±2.49  | 27.28±2.25        | 25.38±3.22 | <b>28.12±3.31</b> | 27.00±2.47         |
| Accuracy/carrot IoU          | 9.77±4.61   | 12.50±5.00        | 9.03 ±4.95 | 17.51±3.81        | <b>24.50±1.05*</b> |
| Accuracy/cat IoU             | 49.25±1.66  | 53.59±1.46        | 49.26±4.30 | 54.25±3.10        | <b>58.75±0.57*</b> |
| Accuracy/ceiling-other IoU   | 37.91±2.53  | 40.41±2.51        | 38.60±1.20 | 38.12±1.77        | <b>43.78±1.67*</b> |
| Accuracy/ceiling-tile IoU    | 0.46±0.69   | <b>2.12 ±2.93</b> | 0.93 ±1.26 | 0.00 ±0.00        | 1.79 ±1.79         |
| Accuracy/cell phone IoU      | 17.72±6.60  | 25.32±3.57        | 15.53±3.03 | 30.42±1.45        | <b>31.71±3.49</b>  |
| Accuracy/chair IoU           | 11.57±0.65  | 14.15±0.90        | 12.25±0.60 | 13.92±0.96        | <b>17.18±0.46*</b> |
| Accuracy/clock IoU           | 35.03±6.16  | 36.70±2.61        | 35.26±0.91 | 42.85±2.37        | <b>46.01±3.31</b>  |
| Accuracy/cloth IoU           | 0.70±0.49   | 0.61 ±0.42        | 0.77 ±0.41 | 0.89 ±0.61        | <b>1.71 ±0.80</b>  |
| Accuracy/clothes IoU         | 0.34±0.35   | 0.39 ±0.54        | 0.20 ±0.21 | <b>0.90 ±0.30</b> | 0.90 ±0.73         |
| Accuracy/clouds IoU          | 35.50±3.45  | 38.24±1.29        | 36.52±0.71 | <b>38.78±1.55</b> | 36.53±1.19         |
| Accuracy/couch IoU           | 20.62±2.11  | 25.54±1.00        | 22.99±0.74 | 27.17±1.24        | <b>31.03±1.03*</b> |
| Accuracy/counter IoU         | 8.21±1.10   | 9.49 ±1.45        | 7.52 ±1.10 | 10.77±0.91        | <b>12.01±0.80*</b> |
| Accuracy/cow IoU             | 26.62±2.21  | 33.73±1.75        | 25.55±2.58 | 32.47±2.17        | <b>42.31±2.17*</b> |
| Accuracy/cup IoU             | 13.61±1.68  | 16.60±2.11        | 14.88±0.60 | 18.38±1.46        | <b>22.35±2.03*</b> |
| Accuracy/cupboard IoU        | 2.14±0.63   | 2.07 ±0.47        | 2.03 ±0.50 | 2.33 ±0.44        | <b>2.99 ±0.41*</b> |
| Accuracy/curtain IoU         | 25.06±2.09  | 25.02±1.60        | 22.93±1.29 | 28.27±3.00        | <b>31.63±1.01*</b> |
| Accuracy/desk-stuff IoU      | 15.88±5.89  | 19.08±2.70        | 15.71±1.20 | 20.15±0.68        | <b>20.22±3.01</b>  |
| Accuracy/dining table IoU    | 27.84±1.14  | 29.65±1.07        | 28.43±1.44 | <b>30.65±1.24</b> | 30.57±1.10         |
| Accuracy/dirt IoU            | 23.10±1.40  | 25.04±2.28        | 23.32±0.55 | 25.59±1.14        | <b>25.66±1.33</b>  |
| Accuracy/dog IoU             | 31.39±3.86  | 35.85±2.10        | 29.77±2.92 | 40.65±2.12        | <b>46.68±2.94*</b> |
| Accuracy/donut IoU           | 10.76±4.61  | 22.40±4.03        | 18.05±7.42 | 31.87±2.00        | <b>33.74±2.96</b>  |
| Accuracy/door-stuff IoU      | 7.55±2.00   | 8.81 ±2.36        | 9.32 ±2.05 | 10.34±1.85        | <b>14.51±1.43*</b> |
| Accuracy/elephant IoU        | 62.90±2.87  | 69.92±2.57        | 62.43±5.71 | 70.44±2.81        | <b>72.27±1.52</b>  |
| Accuracy/fence IoU           | 22.23±0.84  | 23.69±1.36        | 21.91±0.86 | 22.18±0.55        | <b>24.27±0.85</b>  |
| Accuracy/fire hydrant IoU    | 36.19±3.30  | 48.32±1.73        | 38.82±4.21 | 52.31±4.77        | <b>53.39±3.65</b>  |
| Accuracy/floor-marble IoU    | 0.07±0.16   | 0.06 ±0.07        | 0.13 ±0.29 | 0.09 ±0.12        | <b>0.78 ±0.76</b>  |
| Accuracy/floor-other IoU     | 7.21±1.96   | 8.57 ±0.95        | 7.76 ±1.44 | 8.33 ±1.07        | <b>9.72 ±1.01</b>  |
| Accuracy/floor-stone IoU     | 0.87±1.44   | 0.47 ±0.33        | 1.42 ±1.74 | 0.96 ±0.72        | <b>2.19 ±2.62</b>  |
| Accuracy/floor-tile IoU      | 27.01±2.41  | 30.65±1.63        | 26.48±2.93 | 30.73±1.17        | <b>34.09±1.49*</b> |
| Accuracy/floor-wood IoU      | 27.66±1.34  | 30.17±2.20        | 27.28±2.14 | 30.50±0.88        | <b>33.86±1.04*</b> |
| Accuracy/flower IoU          | 13.11±3.94  | 13.15±3.50        | 15.08±1.77 | 15.67±4.07        | <b>17.83±3.72</b>  |
| Accuracy/fog IoU             | 0.00±0.00   | 0.00 ±0.00        | 0.00 ±0.00 | 0.00 ±0.00        | <b>0.90 ±1.48</b>  |
| Accuracy/food-other IoU      | 11.00±2.01  | 11.00±2.86        | 11.71±1.61 | 15.72±2.33        | <b>15.73±3.23</b>  |
| Accuracy/fork IoU            | 0.02±0.04   | 0.09 ±0.19        | 0.10 ±0.21 | 0.46 ±0.47        | <b>8.52 ±1.34*</b> |
| Accuracy/frisbee IoU         | 13.83±1.21  | 17.55±4.16        | 16.34±1.48 | 22.86±4.01        | <b>24.51±2.49</b>  |
| Accuracy/fruit IoU           | 5.91±3.66   | 6.88 ±3.33        | 2.70 ±1.90 | 7.76 ±2.38        | <b>11.88±2.45*</b> |
| Accuracy/furniture-other IoU | 3.44±0.50   | 4.82 ±0.41        | 4.40 ±0.38 | 3.81 ±0.91        | <b>5.21±1.05</b>   |
| Accuracy/giraffe IoU         | 58.36±3.01  | 63.92±1.85        | 60.09±3.61 | 64.29±0.55        | <b>67.67±1.93*</b> |
| Accuracy/grass IoU           | 55.90±0.87  | <b>58.86±0.69</b> | 55.42±1.52 | 57.43±0.91        | 58.25±1.10         |
| Accuracy/gravel IoU          | 7.83±0.80   | <b>7.30 ±0.69</b> | 5.59 ±2.22 | 5.80 ±0.95        | 6.46 ±2.18         |
| Accuracy/ground-other IoU    | 3.25±0.28   | 3.80 ±0.47        | 3.24 ±0.71 | 2.89 ±0.83        | <b>3.82 ±0.76</b>  |
| Accuracy/hair drier IoU      | 0.00±0.00   | 0.00 ±0.00        | 0.00 ±0.00 | 0.00 ±0.00        | 0.00 ±0.00         |
| Accuracy/handbag IoU         | 0.28±0.24   | 0.60 ±0.17        | 0.47 ±0.38 | 0.49 ±0.31        | <b>1.53 ±0.84*</b> |
| Accuracy/hill IoU            | 8.99±1.51   | <b>9.35 ±0.89</b> | 7.18 ±1.46 | 9.28 ±0.84        | 9.02 ±1.15         |
| Accuracy/horse IoU           | 30.17±3.93  | 36.97±3.73        | 33.47±2.96 | 35.01±2.94        | <b>44.53±4.28*</b> |
| Accuracy/hot dog IoU         | 14.85±2.54  | 21.71±4.69        | 17.86±4.90 | 23.08±3.74        | <b>28.67±2.12*</b> |
| Accuracy/house IoU           | 8.39±2.52   | 6.87 ±1.06        | 8.59 ±1.97 | 6.43 ±2.20        | <b>11.28±2.41*</b> |
| Accuracy/keyboard IoU        | 33.86±3.03  | 31.90±3.16        | 30.97±4.11 | 35.82±2.19        | <b>38.76±2.88</b>  |
| Accuracy/kite IoU            | 16.28±4.54  | 18.20±3.38        | 15.68±2.51 | 17.73±4.33        | <b>23.85±3.21*</b> |
| Accuracy/knife IoU           | 0.18±0.39   | 0.29 ±0.49        | 0.18 ±0.39 | 0.35 ±0.22        | <b>4.97 ±0.72*</b> |
| Accuracy/laptop IoU          | 28.13±2.03  | 32.85±2.16        | 28.67±1.85 | 32.85±2.66        | <b>42.55±0.97*</b> |
| Accuracy/leaves IoU          | 4.15±3.03   | <b>6.62 ±5.49</b> | 4.38 ±2.23 | 3.66 ±3.35        | 4.85 ±2.61         |
| Accuracy/light IoU           | 3.36±1.75   | 5.77 ±0.70        | 2.39 ±1.55 | 5.24 ±2.57        | <b>12.25±1.09*</b> |

Continued on next page

## Mining of Single-Class by Active Learning for Semantic Segmentation

| Class                         | Random 2.5% | Random 5%         | Entropy 5% | BALD 5%            | MiSiCAL 5%         |
|-------------------------------|-------------|-------------------|------------|--------------------|--------------------|
| Accuracy/mat IoU              | 0.00±0.00   | 0.05 ±0.09        | 0.00 ±0.00 | 0.10 ±0.19         | <b>0.51 ±1.14</b>  |
| Accuracy/metal IoU            | 1.51±0.92   | 2.14 ±0.74        | 1.08 ±0.31 | <b>2.40 ±1.18</b>  | 2.21 ±0.44         |
| Accuracy/microwave IoU        | 5.94±6.74   | 10.60±4.45        | 4.60 ±4.37 | 17.99±2.17         | <b>21.40±3.91</b>  |
| Accuracy/mirror-stuff IoU     | 8.80±1.64   | 12.93±2.12        | 5.78 ±2.58 | 10.63±1.60         | <b>17.80±1.26*</b> |
| Accuracy/moss IoU             | 0.00±0.00   | 0.00 ±0.00        | 0.00 ±0.00 | 0.00 ±0.00         | 0.00 ±0.00         |
| Accuracy/motorcycle IoU       | 48.67±3.03  | 52.46±0.94        | 50.20±1.12 | 49.95±2.74         | <b>57.83±0.58*</b> |
| Accuracy/mountain IoU         | 25.52±3.16  | 30.27±3.33        | 24.76±5.51 | 23.27±2.89         | <b>32.41±3.20</b>  |
| Accuracy/mouse IoU            | 2.57±3.69   | 10.97±10.69       | 4.83 ±4.14 | 20.80±1.07         | <b>24.42±4.12</b>  |
| Accuracy/mud IoU              | 0.63±1.01   | 1.51 ±1.89        | 0.19 ±0.29 | 0.02 ±0.05         | <b>2.81 ±0.96</b>  |
| Accuracy/napkin IoU           | 0.00±0.00   | 0.03 ±0.07        | 0.51 ±0.83 | 0.09 ±0.18         | <b>4.40 ±3.69*</b> |
| Accuracy/net IoU              | 13.38±4.80  | 17.32±3.16        | 9.90 ±2.91 | 11.34±2.45         | <b>19.98±4.45</b>  |
| Accuracy/orange IoU           | 31.91±3.90  | 37.38±3.33        | 32.77±2.83 | 43.34±2.67         | <b>47.93±2.58*</b> |
| Accuracy/oven IoU             | 22.52±1.30  | 26.82±1.14        | 22.10±2.31 | 27.82±2.07         | <b>32.65±1.79*</b> |
| Accuracy/paper IoU            | 3.20±1.07   | 5.57 ±1.49        | 3.53 ±1.23 | 3.74 ±0.61         | <b>7.20 ±1.35</b>  |
| Accuracy/parking meter IoU    | 11.61±3.52  | 19.63±2.93        | 14.09±4.21 | 29.42±4.99         | <b>30.82±5.23</b>  |
| Accuracy/pavement IoU         | 28.06±1.94  | <b>27.84±1.80</b> | 25.95±2.04 | 26.03±1.05         | 27.06±1.59         |
| Accuracy/person IoU           | 63.99±0.90  | 66.49±0.41        | 63.82±1.29 | <b>66.77±0.91</b>  | 65.69±1.35         |
| Accuracy/pillow IoU           | 0.06±0.14   | 0.00 ±0.00        | 0.00 ±0.00 | 0.00 ±0.00         | <b>0.00 ±0.01</b>  |
| Accuracy/pizza IoU            | 42.23±4.71  | 46.33±1.71        | 44.91±3.28 | 48.84±3.59         | <b>53.03±1.01*</b> |
| Accuracy/plant-other IoU      | 10.16±1.07  | <b>10.73±0.88</b> | 9.16 ±1.64 | 10.62±1.30         | 10.49±1.75         |
| Accuracy/plastic IoU          | 0.36±0.43   | 0.09 ±0.09        | 0.28 ±0.24 | 0.58 ±0.42         | <b>1.61 ±0.63*</b> |
| Accuracy/platform IoU         | 11.32±2.88  | 15.32±1.90        | 11.32±3.32 | 13.29±1.80         | <b>17.78±0.54*</b> |
| Accuracy/playingfield IoU     | 56.43±1.68  | 55.06±3.43        | 53.96±4.16 | <b>56.79±1.01</b>  | 56.24±4.21         |
| Accuracy/potted plant IoU     | 13.02±1.96  | 16.01±1.05        | 12.84±1.87 | 16.48±2.37         | <b>16.74±1.05</b>  |
| Accuracy/railing IoU          | 1.11±0.17   | 1.52 ±0.30        | 1.02 ±0.16 | 0.95 ±0.28         | <b>1.76 ±0.45</b>  |
| Accuracy/railroad IoU         | 35.85±5.60  | 41.37±0.78        | 36.99±2.27 | 40.32±0.91         | <b>42.89±3.01</b>  |
| Accuracy/refrigerator IoU     | 18.70±1.46  | 22.91±2.59        | 21.19±2.56 | 29.80±2.95         | <b>42.31±2.42*</b> |
| Accuracy/remote IoU           | 5.50±4.17   | 8.02 ±4.72        | 5.54 ±2.90 | <b>17.46±3.19</b>  | 12.28±8.52         |
| Accuracy/river IoU            | 8.15±2.37   | 10.26±1.21        | 10.98±6.61 | 9.64 ±4.60         | <b>13.00±3.01</b>  |
| Accuracy/road IoU             | 38.82±5.27  | 42.56±0.49        | 40.87±0.62 | 42.28±0.49         | <b>44.53±1.97*</b> |
| Accuracy/rock IoU             | 24.51±2.86  | 30.69±2.70        | 27.22±2.47 | 29.13±1.58         | <b>31.59±1.77</b>  |
| Accuracy/roof IoU             | 4.28±0.82   | 4.96 ±2.16        | 3.35 ±1.80 | 3.78 ±1.13         | <b>6.45 ±1.99</b>  |
| Accuracy/rug IoU              | 6.97±0.65   | 9.69 ±1.03        | 6.03 ±1.50 | 8.78 ±1.42         | <b>12.55±1.53*</b> |
| Accuracy/salad IoU            | 1.54±1.99   | 1.26 ±2.00        | 0.85 ±1.46 | 0.96 ±0.72         | <b>7.90 ±3.53*</b> |
| Accuracy/sand IoU             | 36.70±2.05  | 37.48±2.51        | 35.99±2.42 | 36.37±0.86         | <b>39.66±0.97</b>  |
| Accuracy/sandwich IoU         | 17.46±2.36  | 18.47±2.63        | 16.80±2.39 | 19.21±1.57         | <b>23.38±2.53*</b> |
| Accuracy/scissors IoU         | 4.13±5.10   | 13.34±2.74        | 7.08 ±5.32 | <b>24.25±5.72*</b> | 16.59±6.84         |
| Accuracy/sea IoU              | 67.76±1.34  | 70.46±1.68        | 70.09±0.80 | 69.79±2.20         | <b>71.60±2.12</b>  |
| Accuracy/sheep IoU            | 35.47±4.03  | 42.74±1.89        | 36.45±3.94 | 49.42±1.74         | <b>50.12±3.48</b>  |
| Accuracy/shelf IoU            | 3.41±1.64   | 5.45 ±1.58        | 2.47 ±1.60 | 8.79 ±2.44         | <b>10.42±1.16</b>  |
| Accuracy/sink IoU             | 24.56±3.81  | 26.56±3.49        | 21.32±4.61 | 29.87±3.13         | <b>34.75±1.23*</b> |
| Accuracy/skateboard IoU       | 3.34±1.97   | 6.22 ±1.88        | 4.93 ±2.53 | 7.52 ±3.71         | <b>16.23±1.24*</b> |
| Accuracy/skis IoU             | 1.11±1.07   | 1.77 ±1.42        | 0.91 ±0.92 | 0.30 ±0.56         | <b>10.98±3.10*</b> |
| Accuracy/sky-other IoU        | 53.69±3.02  | 55.74±3.18        | 54.18±3.03 | <b>57.92±1.44</b>  | 55.58±2.93         |
| Accuracy/skyscraper IoU       | 1.65±2.44   | 3.60 ±2.15        | 1.80 ±1.52 | 1.54 ±2.14         | <b>5.81 ±1.03*</b> |
| Accuracy/snow IoU             | 70.74±2.55  | 74.50±2.45        | 72.22±2.23 | 73.53±0.96         | <b>75.61±1.79</b>  |
| Accuracy/snowboard IoU        | 1.06±1.73   | 3.45 ±1.79        | 2.77 ±1.68 | 2.79 ±3.44         | <b>13.15±3.02*</b> |
| Accuracy/solid-other IoU      | 0.00±0.00   | 0.00 ±0.00        | 0.00 ±0.00 | 0.00 ±0.00         | 0.00 ±0.00         |
| Accuracy/spoon IoU            | 0.00±0.00   | 0.19 ±0.43        | 0.09 ±0.20 | 1.74 ±1.96         | <b>3.68 ±1.78</b>  |
| Accuracy/sports ball IoU      | 1.54±3.28   | 4.22 ±4.13        | 1.55 ±2.52 | 5.61 ±3.92         | <b>15.93±4.82*</b> |
| Accuracy/stairs IoU           | 1.45±1.71   | 1.85 ±0.69        | 0.79 ±1.08 | 2.04 ±1.34         | <b>6.38 ±1.63*</b> |
| Accuracy/stone IoU            | 0.82±0.65   | 0.79 ±0.60        | 1.82 ±2.33 | <b>2.77 ±2.46</b>  | 2.31 ±1.13         |
| Accuracy/stop sign IoU        | 55.99±6.10  | <b>66.04±2.88</b> | 56.00±1.38 | 63.39±7.26         | 63.45±2.91         |
| Accuracy/straw IoU            | 4.92±3.25   | 8.18 ±3.40        | 8.16 ±5.69 | 8.46 ±3.37         | <b>13.80±2.30*</b> |
| Accuracy/structural-other IoU | 0.46±0.13   | <b>0.84 ±0.21</b> | 0.63 ±0.09 | 0.77 ±0.06         | 0.64 ±0.16         |
| Accuracy/suitcase IoU         | 15.31±4.49  | 23.12±2.91        | 17.22±3.11 | 25.97±2.44         | <b>28.88±1.04*</b> |

Continued on next page

## Mining of Single-Class by Active Learning for Semantic Segmentation

| Class                      | Random 2.5% | Random 5%         | Entropy 5% | BALD 5%           | MiSiCAL 5%         |
|----------------------------|-------------|-------------------|------------|-------------------|--------------------|
| Accuracy/surfboard IoU     | 19.42±4.73  | 23.38±4.33        | 14.48±4.69 | 30.07±4.94        | <b>32.52±4.82</b>  |
| Accuracy/table IoU         | 8.96±1.26   | 9.12 ±0.79        | 7.67 ±0.96 | 8.42 ±1.68        | <b>11.23±1.14*</b> |
| Accuracy/teddy bear IoU    | 37.01±2.91  | 42.20±1.91        | 37.67±1.25 | 48.21±1.87        | <b>48.31±1.11</b>  |
| Accuracy/tennis racket IoU | 19.29±5.04  | 23.63±2.90        | 15.95±4.95 | 33.10±7.09        | <b>36.49±3.53</b>  |
| Accuracy/tent IoU          | 0.33±0.46   | 0.51 ±0.68        | 0.05 ±0.11 | 0.48 ±0.58        | <b>0.88 ±0.56</b>  |
| Accuracy/textile-other IoU | 2.00±0.83   | 2.77 ±0.81        | 1.96 ±0.54 | <b>3.46 ±1.11</b> | 3.37 ±0.86         |
| Accuracy/tie IoU           | 0.00±0.00   | 0.00 ±0.00        | 0.00 ±0.00 | 0.00 ±0.00        | <b>0.08 ±0.16</b>  |
| Accuracy/toaster IoU       | 0.00±0.00   | 0.00 ±0.00        | 0.00 ±0.00 | 0.01 ±0.02        | <b>0.73 ±1.13</b>  |
| Accuracy/toilet IoU        | 38.10±2.73  | 43.13±2.51        | 38.22±3.63 | 45.48±1.86        | <b>47.52±3.01</b>  |
| Accuracy/toothbrush IoU    | 0.00±0.00   | <b>0.59 ±1.33</b> | 0.05 ±0.10 | 0.05 ±0.12        | 0.28 ±0.38         |
| Accuracy/towel IoU         | 0.11±0.19   | 0.94 ±1.07        | 0.26 ±0.30 | 0.89 ±0.61        | <b>8.48 ±1.78*</b> |
| Accuracy/traffic light IoU | 20.46±2.13  | 25.43±2.45        | 11.65±6.75 | 22.32±3.58        | <b>31.61±1.77*</b> |
| Accuracy/train IoU         | 41.74±1.10  | 47.41±1.57        | 40.88±3.22 | 44.40±1.55        | <b>51.82±2.72*</b> |
| Accuracy/tree IoU          | 58.77±0.34  | <b>60.50±0.83</b> | 59.03±0.71 | 59.45±0.41        | 59.77±0.42         |
| Accuracy/truck IoU         | 19.17±1.34  | 21.13±2.65        | 19.39±2.09 | 22.19±1.92        | <b>27.45±4.33*</b> |
| Accuracy/tv IoU            | 26.38±2.48  | 29.62±1.58        | 26.50±1.39 | 31.49±1.72        | <b>37.79±3.11*</b> |
| Accuracy/umbrella IoU      | 28.20±3.45  | 30.73±1.35        | 26.20±0.96 | 37.57±2.13        | <b>39.11±1.16</b>  |
| Accuracy/vase IoU          | 15.47±3.79  | 21.86±2.93        | 15.15±3.37 | <b>24.68±2.48</b> | 24.48±3.30         |
| Accuracy/vegetable IoU     | 7.36±4.46   | 8.98 ±1.43        | 8.43 ±3.12 | <b>14.96±2.06</b> | 13.82±1.80         |
| Accuracy/wall-brick IoU    | 18.43±1.40  | 19.53±2.37        | 18.01±1.54 | 19.50±1.37        | <b>20.20±1.30</b>  |
| Accuracy/wall-concrete IoU | 1.50±0.37   | 2.01 ±0.68        | 1.52 ±0.54 | 1.27 ±0.56        | <b>2.41 ±0.67</b>  |
| Accuracy/wall-other IoU    | 8.58±0.27   | 9.01 ±0.49        | 8.88 ±0.40 | 9.05 ±0.30        | <b>9.28 ±0.17</b>  |
| Accuracy/wall-panel IoU    | 0.21±0.14   | <b>0.27 ±0.46</b> | 0.25 ±0.35 | 0.12 ±0.16        | 0.18 ±0.20         |
| Accuracy/wall-stone IoU    | 10.13±2.31  | 9.61 ±2.85        | 10.52±2.03 | 9.48 ±3.22        | <b>12.34±1.88</b>  |
| Accuracy/wall-tile IoU     | 33.72±1.46  | 34.04±2.31        | 32.78±1.86 | 34.61±1.35        | <b>36.84±1.35*</b> |
| Accuracy/wall-wood IoU     | 10.56±2.04  | 13.73±2.02        | 12.13±2.03 | 13.84±1.68        | <b>14.29±2.11</b>  |
| Accuracy/water-other IoU   | 14.34±2.75  | 14.02±1.52        | 14.19±2.50 | <b>15.52±2.81</b> | 14.44±2.86         |
| Accuracy/waterdrops IoU    | 0.01±0.01   | 0.06 ±0.13        | 0.00 ±0.00 | 0.00 ±0.00        | <b>0.81 ±1.00</b>  |
| Accuracy/window-blind IoU  | 15.34±1.79  | 20.84±2.12        | 16.24±2.33 | 20.94±1.01        | <b>23.17±1.48*</b> |
| Accuracy/window-other IoU  | 19.47±1.65  | 21.83±0.85        | 19.48±0.60 | 21.75±0.84        | <b>23.66±1.21*</b> |
| Accuracy/wine glass IoU    | 11.83±6.35  | 18.58±4.20        | 10.70±6.24 | 21.00±4.17        | <b>24.62±1.98</b>  |
| Accuracy/wood IoU          | 3.55±0.56   | 4.45 ±1.55        | 3.49 ±0.92 | 4.44 ±1.23        | <b>5.31 ±0.42</b>  |
| Accuracy/zebra IoU         | 74.49±1.17  | 74.77±2.92        | 73.50±2.68 | <b>75.75±1.65</b> | 74.64±1.73         |

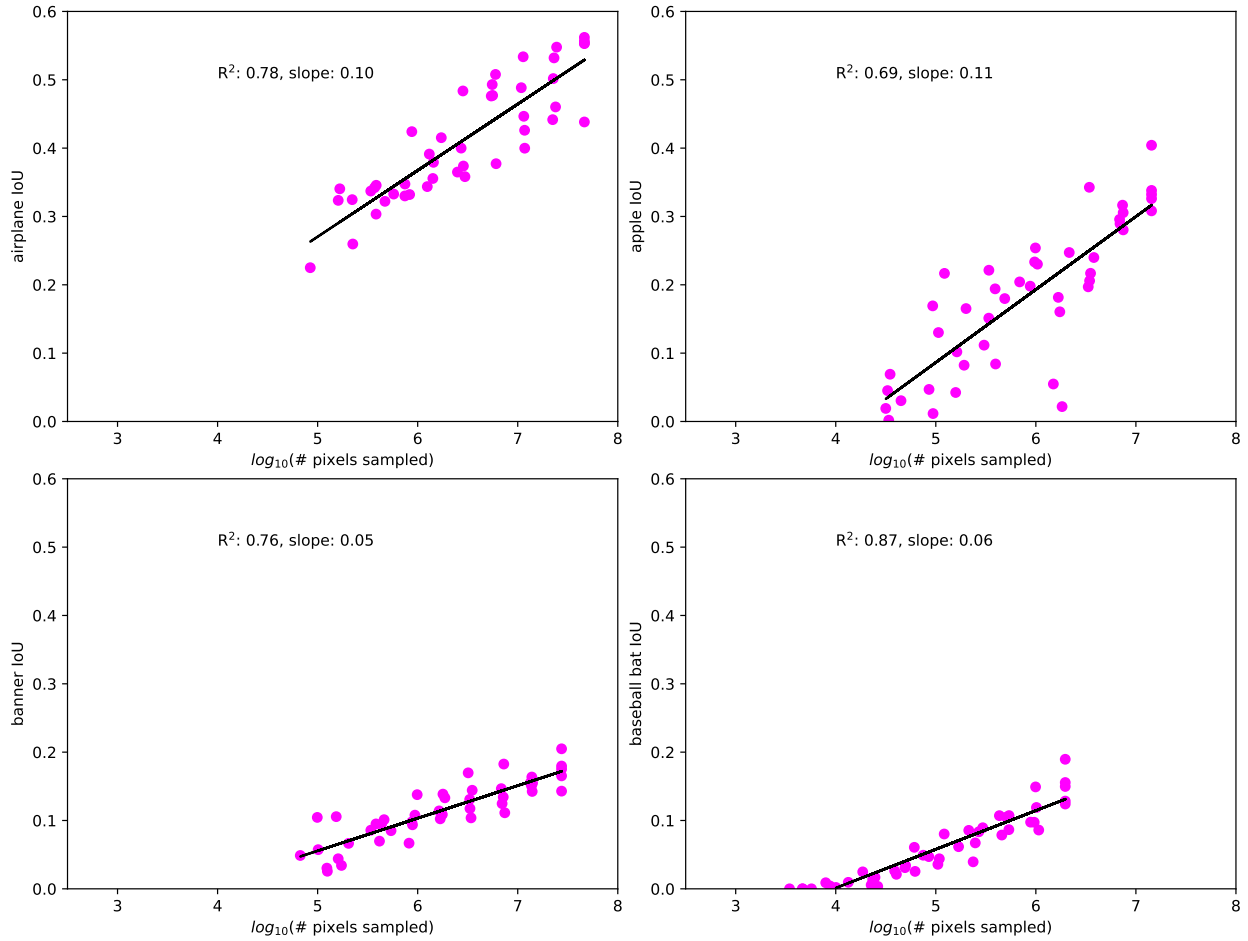


Figure A2: Relationship between the amount of pixels for a class in the training dataset versus the resulting class IoU. The relationship appears linear past a threshold of about  $\log_{10}(\text{pixel count}) = 4.5$ .

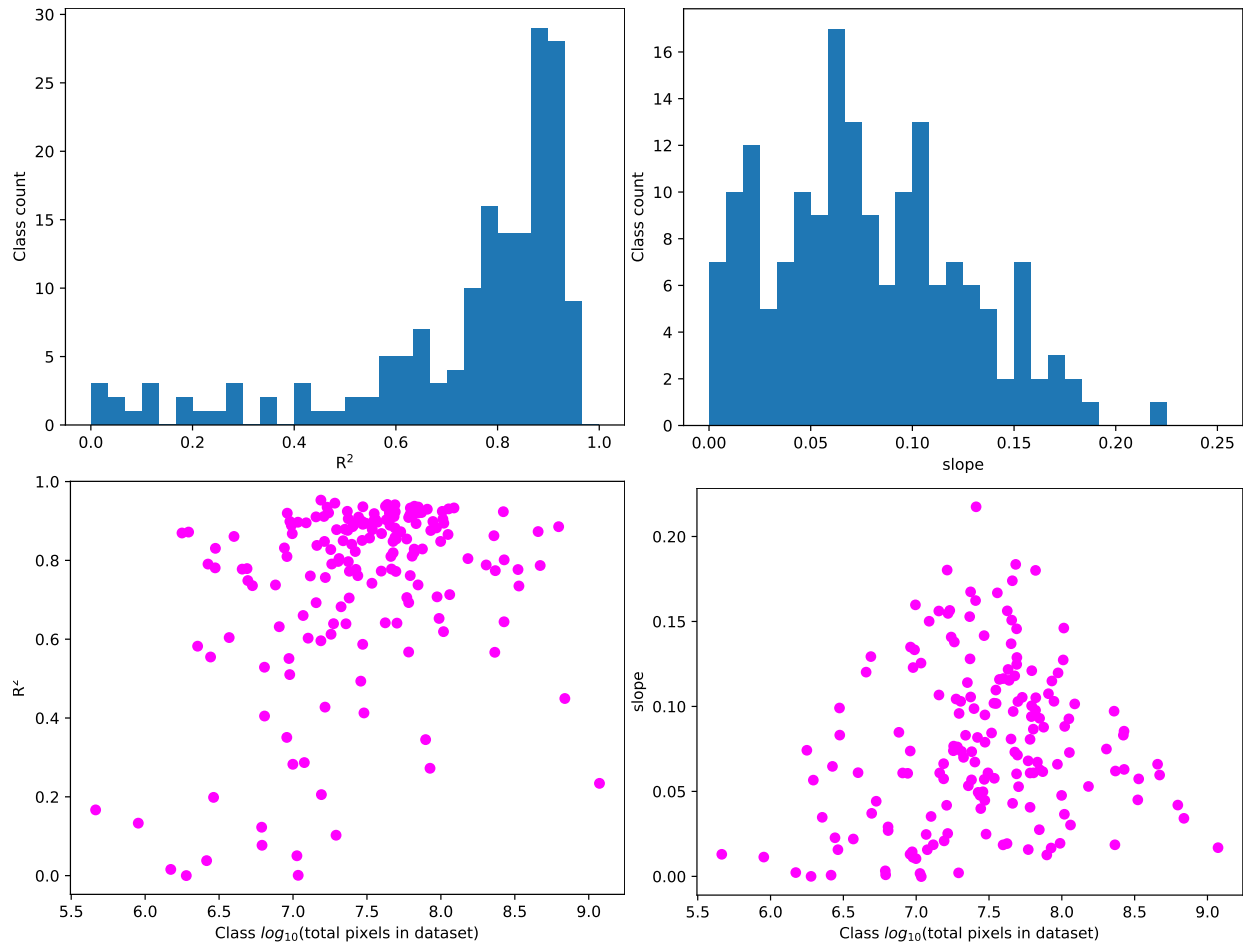


Figure A3: Histogram of the  $R^2$ , slopes values of the class pixel counts versus their IoU. It appears that over half of all classes exhibit a linear pixel count vs IoU correlation with a  $R^2$  value superior to 0.8. On the other hand the value of the regression slopes are more uniformly spread in the 0 to 0.25 range. There does not seem to be a correlation between the total number of pixels from a class in the dataset with either  $R^2$  nor the slopes values.

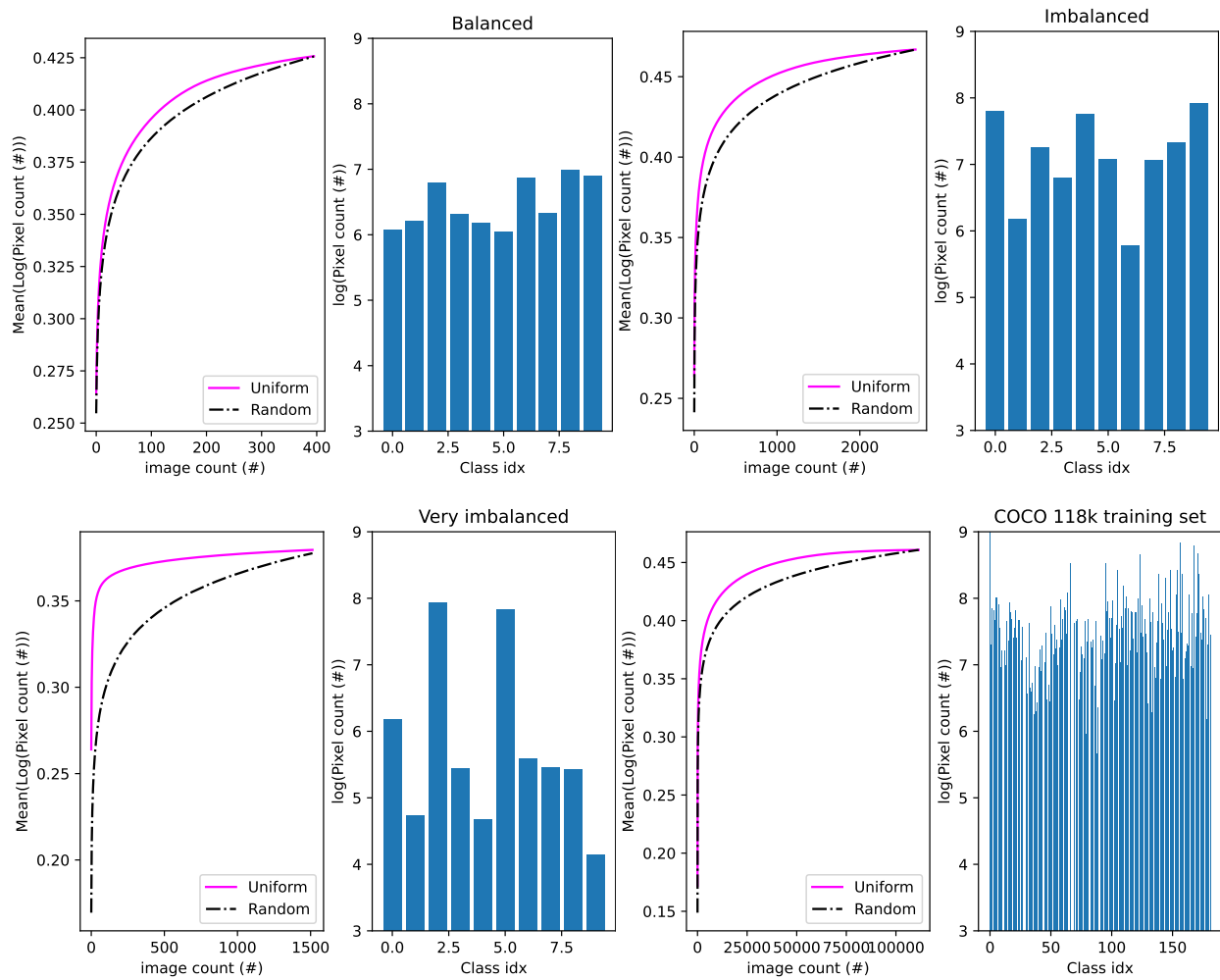


Figure A4: Evolution of the mean IoU corresponding to a class uniform versus random sampling of a pixel distribution and assuming a linear relationship between the logarithm of the amount of pixels of a specific class in the training dataset and its IoU.

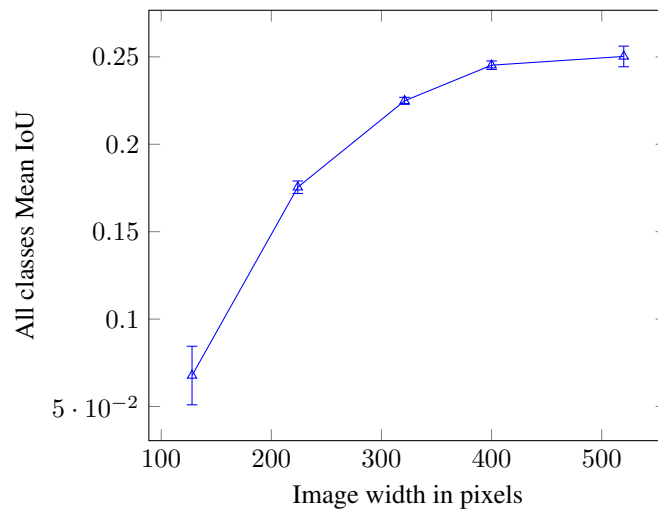


Figure A5: Evolution of the accuracy of the segmentation model with regard to the input image size for a sample of 10,000 images from the COCO164k training dataset. It appears that using larger images leads to higher end accuracies. Images are augmented according to the procedure described in 3.2. Test images are the 5,000 COCO164k validation images and are resized to the same size as the training images. The images are used whole and not cut into patches. All runs are trained for a maximum of 50 epochs with a cosine annealing learning rate schedule with a 50 epochs period and starting at 0.001 with a minimum of 0. An early stopping criterion of the all class Mean IoU with patience of 5 epochs. Error bars are the standard deviation for 5 seeds.

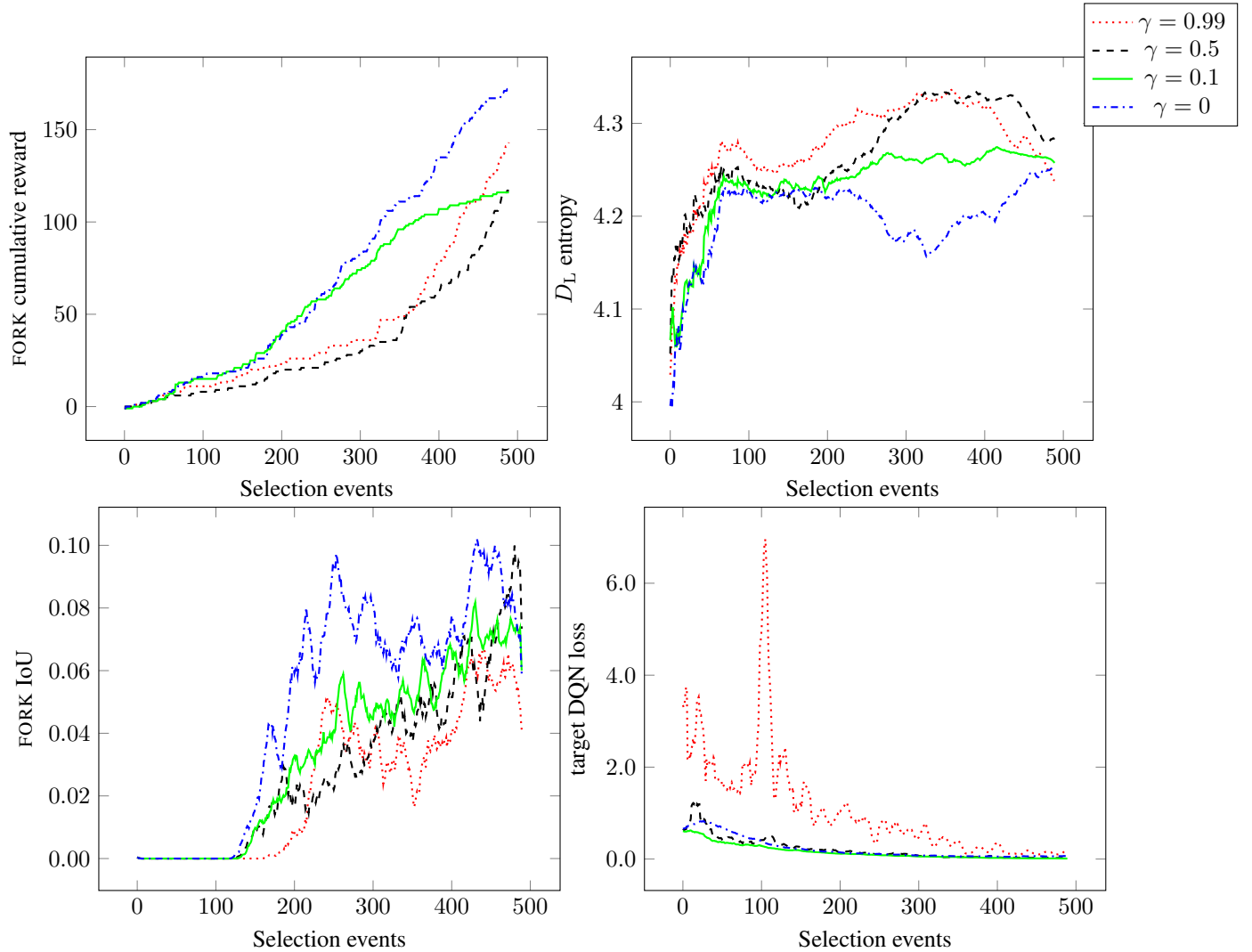


Figure A6: Influence of the discount factor  $\gamma$  on the behaviour of the DDQN. At  $\gamma = 0$ , the agent picks early on patches containing FORK pixels while at higher  $\gamma$  values, more selection events are required to select the patches leading to rewards. This focus on the patches associated with the reward leads to a diminution of the entropy of the  $D_L$  pixel histogram for smaller values of  $\gamma$ . For larger discount factors, the agent tends to pick patches containing more diverse pixels. The target DQN loss is very stable for low discount factors and becomes progressively less so for higher values of  $\gamma$ . Interestingly, while picking the most patches and doing so earlier, the run with  $\gamma = 0$  does not lead to a much higher FORK IoU at the end of the selection procedure. This is presumably because the more diverse datasets picked by agents with a higher discount factor help the segmentation model to build better features. At each sampling event, 64 patches are selected from a random selection of 1280 patches, then added to  $D_L$  and one epoch of training is performed on the whole  $D_L$ . The process is repeated until 5% of  $D_U$  (COCO10k) has been picked and only 250 patches are initially randomly sampled and added to  $D_L$ . An  $\epsilon$  annealing is applied from 1 to 0.1 over 500 steps. The DDQN batch size is set to 256 while the buffer contains 6400 experiences. Rewards are granted when the agent picks FORK-containing patches. The soft update is performed with  $\beta = 0.002$ .

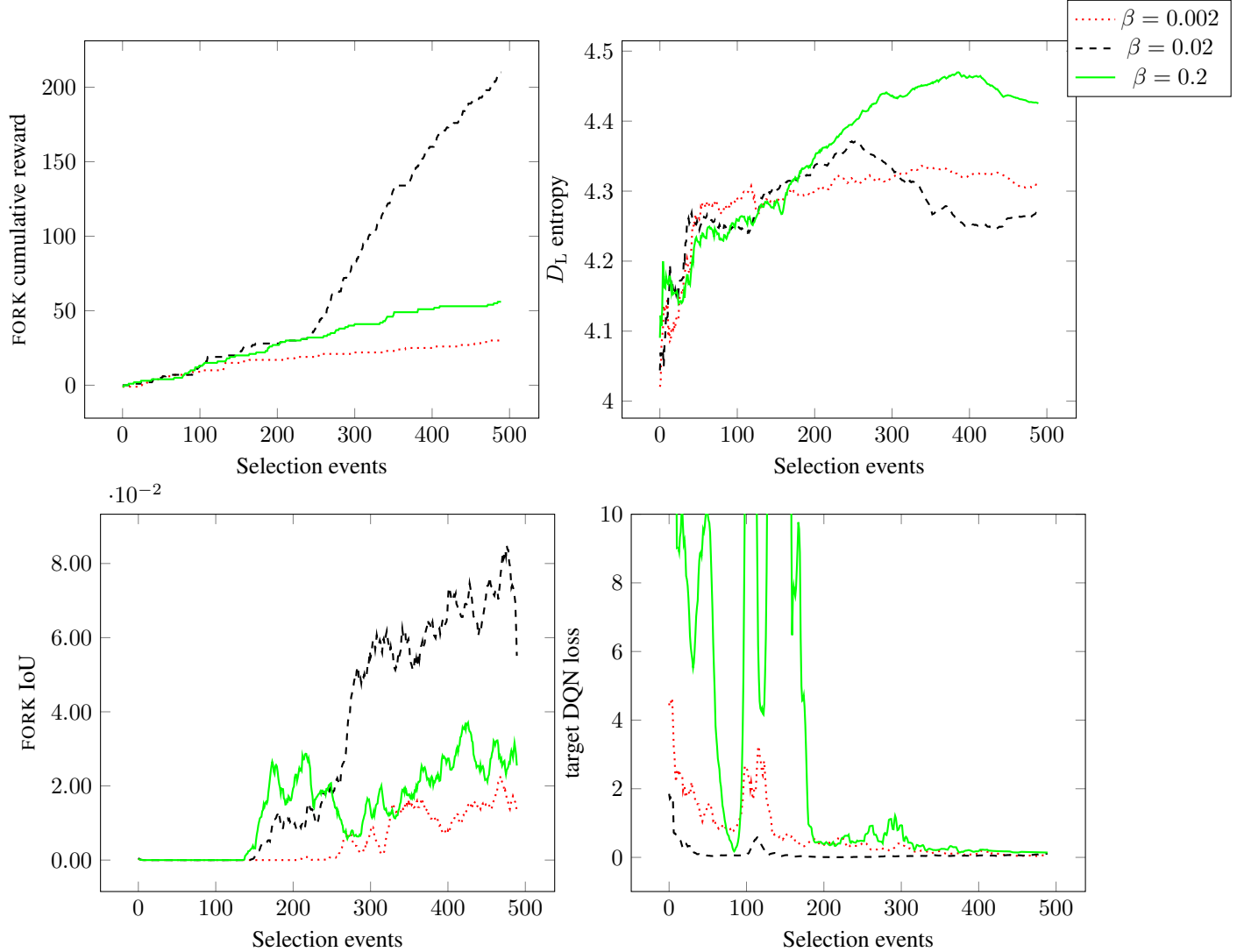


Figure A7: A soft update carried out too aggressively with high  $\beta$  values leads to instabilities, while a soft update too slow means the network is not updating its Q-value estimates fast enough and learns slower. The loss of the target DQN in the case  $\beta = 0.2$  loss goes up to 300 but this is cropped on the image. At each sampling event, 64 patches are selected from a random selection of 1280 patches, then added to  $D_L$  and one epoch of training is performed on the whole  $D_L$ . The process is repeated until 5% of  $D_U$  (COCO10k) has been picked and only 250 patches are initially randomly sampled and added to  $D_L$ . An  $\epsilon$  annealing is applied from 1 to 0.1 over 250 steps. The DDQN batch size is set to 256 while the buffer contains 6400 experiences. The discount factor  $\gamma$  is set to 0.99. Rewards are granted when the agent picks FORK-containing patches. Gradients are clipped to 0.01.

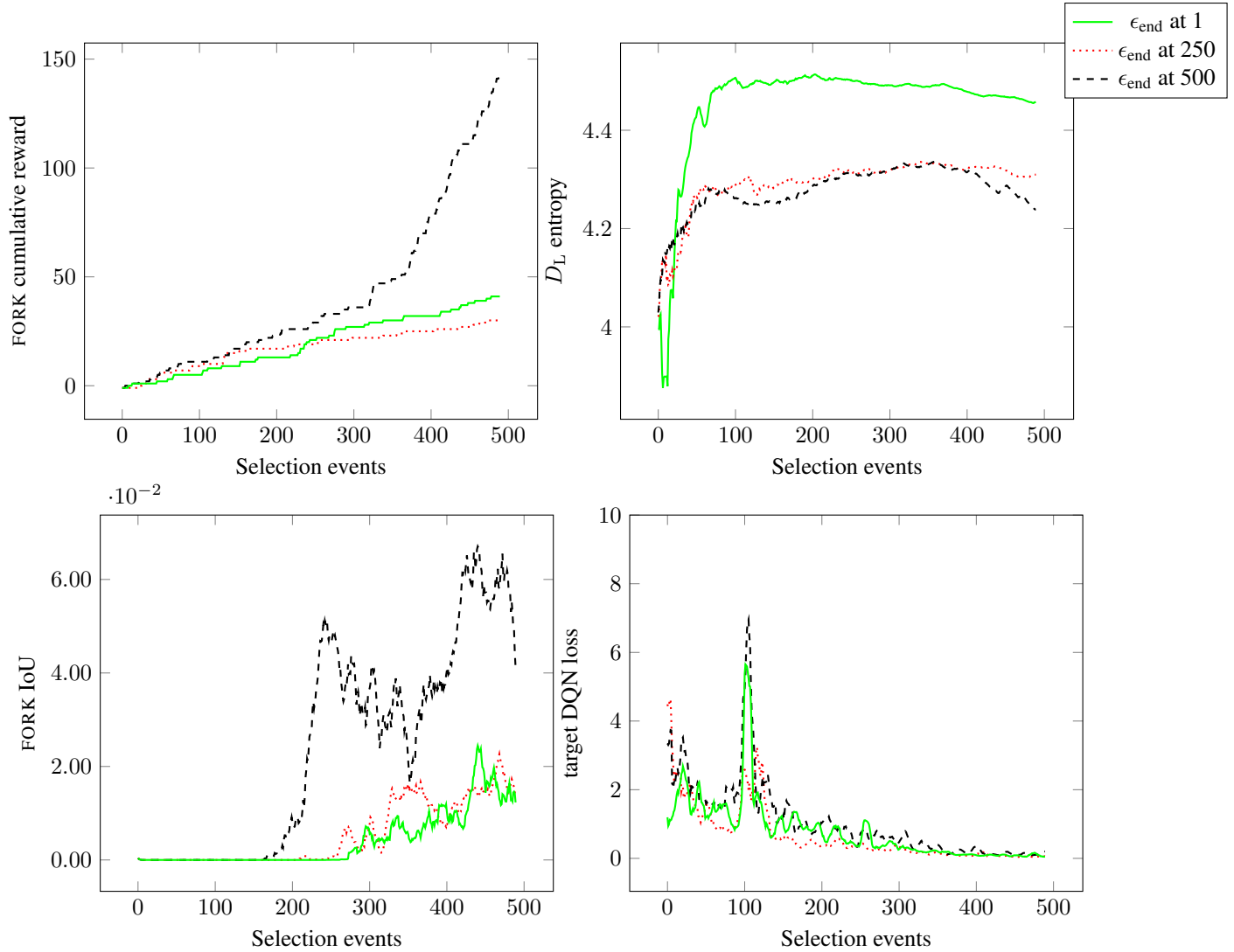


Figure A8: Different  $\epsilon$ -annealing schedules, where the probability of picking patches at random decreases from 1 to  $\epsilon_{\text{end}}$  (here 0.1), lead to different behaviours and DDQN performances. Not performing an  $\epsilon$ -annealing, where  $\epsilon_{\text{end}}$  is reached at the first step, leads to the model directly having to pick patches without having much information and trying to exploit lacunary knowledge. This can be problematic for relatively rare classes like FORK since finding enough patches to build an effective policy requires significant sampling initially. At each sampling event, 64 patches are selected from a random selection of 1280 patches, then added to  $D_L$  and one epoch of training is performed on the whole  $D_L$ . The process is repeated until 5% of  $D_U$  (COCO10k) has been picked and only 250 patches are initially randomly sampled and added to  $D_L$ . The DDQN batch size is set to 256 while the buffer contains 6400 experiences. The discount factor  $\gamma$  is 0.99 while the soft update rate  $\beta$  is 0.002. Rewards are granted when the agent picks FORK-containing patches. Gradients are clipped to 0.01.

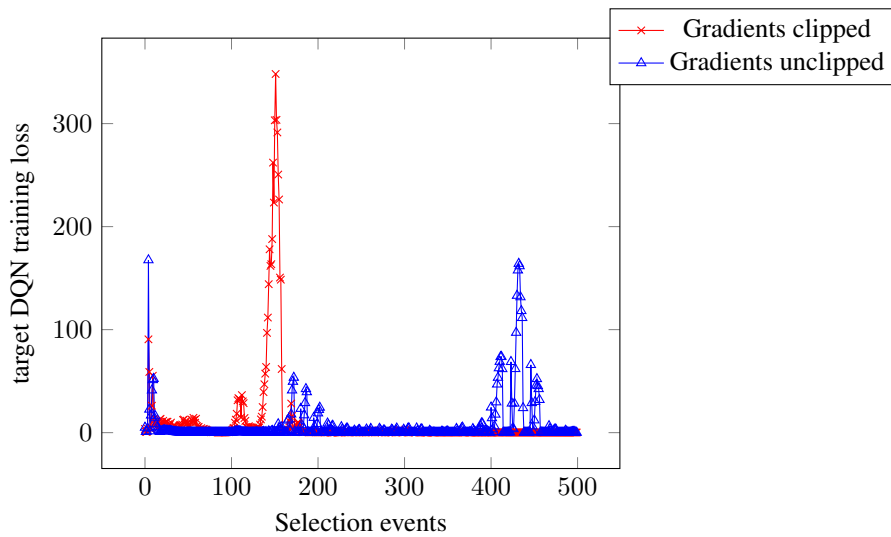


Figure A9: Clipping the gradients does not prevent the Q-values from reaching high values. Using the soft update method from (18) is meant to avoid such instabilities, however when  $\beta$  is set to very high values (here  $\beta = 0.2$ ), instabilities occur and clipping the gradients to 0.01 does not prevent the instabilities from happening. At each sampling event, 64 patches are selected from a random selection of 1280 patches, then added to  $D_L$  and one epoch of training is performed on the whole  $D_L$ . The process is repeated until 5% of  $D_U$  (COCO10k) has been picked and only 250 patches are initially randomly sampled and added to  $D_L$ . An  $\epsilon$ -annealing is applied from 1 to 0.1 over 250 steps with  $\gamma$  set to 0.99. The DDQN batch size is set to 256 while the buffer contains 6400 experiences. Rewards are granted when the agent picks FORK-containing patches.

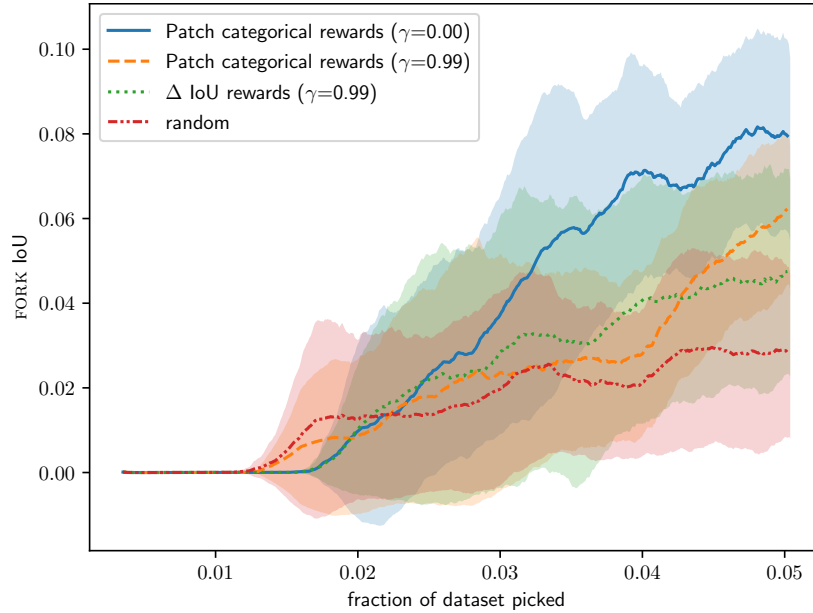


Figure A10: Comparison of using categorical rewards associated with picking a patch containing the class of interest and using rewards linked to the change in IoU of the class of interest ( $\Delta$  IoU). Using  $\gamma = 0$  and categorical rewards leads to the fastest accumulation of FORK-containing patches (4x faster than in the random policy) followed by the same settings with  $\gamma = 0.99$ . Using  $\Delta$  IoU rewards leads to both slow accumulation of FORK-containing patches and slow rise in FORK IoU presumably because the rewards are less granular as all patches selected in a step are assigned the same reward. Curves are the means of 5 seeds with the shading corresponding to their standard deviation, both averaged with a 30 step window. At each sampling event, 64 patches are selected from a random selection of 1280 patches, then added to  $D_L$  and one epoch of training is performed on the whole  $D_L$ . The process is repeated until 5% of  $D_U$  (COCO10k) has been picked and only 250 patches are initially randomly sampled and added to  $D_L$ . An  $\epsilon$ -annealing is applied from 1 to 0.1 over 500 steps, which corresponds to 5% of  $D_U$ . The DDQN batch size is set to 256 while the buffer contains 6400 experiences. The soft update rate  $\beta$  is set to 0.02 and gradients are not clipped.